CENTRO DE INVESTIGACIONES
EN OPTICA, A.C.

“ SECOND HARMONIC GENERATION IN NANOSTRUCTURED METAMATERIALS ”

A thesis to obtain the degree of Doctor of Science (Optics) by

Ulises Ramírez Meza

Advisor: Dr. Bernardo Mendoza Santoyo

Versión definitiva.
Incluye cambios sugeridos por revisores

León · Guanajuato · México
August 2022

B. Mendoza S.

Vo.Bo.

Second Harmonic Generation in Nanostructured Metamaterials

by

Ulises Ramírez Meza

A thesis submitted in partial fulfillment of the requirements

for the degree of Doctor of Philosophy.

Advisor:

Dr. Bernardo Mendoza Santoyo

Centro de Investigaciones en Óptica, A.C.

Loma del Bosque 115, León, Guanajuato, 37150, México

August 24, 2022

The research presented in this thesis was carried out at the Centro de Investigaciones en Óptica, A.C., Loma del Bosque 115, León, Guanajuato, 37150, Mexico, in collaboration with the Instituto de Ciencias Físicas de la UNAM. Funding was provided by the CONACYT-México (Consejo Nacional de Ciencia y Tecnología), through scholarship Nº 589138.

Second Harmonic Generation in Nanostructured Metamaterials

by

Ulises Ramírez Meza

Approved:

Dr. Bernardo Mendoza Santoyo

Thesis Advisor

Centro de Investigaciones en Óptica, A.C.

Loma del Bosque 115, León, Guanajuato, 37150, México

August, 2022

I dedicate this work to my family, Carolina, Tomás and David.

"Sometimes you have to go up really high to understand how small you are."

Felix Baumgartner

Abstract

In this thesis, we conduct a theoretical and numerical study on the second-harmonic (SH) optical response of a nano-structured metamaterial. These metamaterials are composed of a periodic array of both metallic and dielectric inclusions. The inclusions and their surrounding matrix are made of centrosymmetrical materials, for which SH is forbidden in the dipole approximation. With a proper choice of the shape of the inclusions, we may produce a geometrically non-centrosymmetric system which does allow efficient SH generation. The linear and quadratic spectra of the optical response of the metamaterial can be tunned by simple variations in the geometrical configuration of the inclusions.

A theory that allows the calculation of the nonlinear polarization from the geometry of the system and its linear dielectric function at the fundamental and second-harmonic frequencies is developed, and we implement an efficient scheme for its numerical computation. Thus, extending a formalism for the calculation of the macroscopic dielectric function using Haydock's recursion method.

The formalism obtained is used in order to calculate the optical properties of different periodic arrays of nanostructures within metallic and nonmetallic matrices. It can be applied to any combination of materials and geometry for inclusions, within the long-wavelength regime.

Acknowledgements

This thesis is the culmination of a five year path of hard work and personal effort and one of the most sifnificant stages in my life. Many people have been involved in this journey in different ways, at various stages; I can't be more than grateful to all of them.

Firstable, I want to thank my advisor, Dr. Bernardo Mendoza Santoyo, for his willingness to share all his knowledge with me. But, above all, for the patience and commitment he had with me. They were years of hard work and learning, which without a doubt, would not have been the same without their accompaniment.

I extend these thanks to Dr. Laura Rosales, Dr. Norberto Arzate, Dr. Ramón Carriles for their pertinent comments on this work and during the predictive evaluation. In this same sense, I want to thank Dr. Luis Mochán for these years of collaboration and teachings. Special thanks to each of the CIO researchers from whom I had the opportunity to take classes at some point in my postgraduate studies.

To all my colleagues with whom I had the pleasure of working within the CIO, someone became unconditional friends through time. To my friends inside and outside the CIO, from whom I received nothing but support when I most needed it. I would not want to leave any of you out; Thank you all for being with me at this stage.

I am grateful towards the CONACyT and the CIO for the financial support and infrastructure contributed towards this work.

I would like to thank my family; to my mother, Carolina, my father, Tomás and my brother, David. You have always found a way. You had give me your unconditional support, regardless of the circumstance, including the sacrifices that this implied. I owe you a lot.

Finally, I would like to thank each of the people who have been with me throughout these years; who are now, who have joined, and also those who are no longer. Each one represents a relevant part in the journey of this path.

Contents

List of Figures

1 Introduction

1.1 Metamaterials

In recent years, nanophotonics has emerged as a fruitful sub-branch of photonics that deals with the phenomena involved in light-matter interaction at the nanoscale. [1] The enormous advances in this area have been reflected in a wide literature about materials properties and their behavior when interaction with light is present. [2, 3] In this way, optical metamaterials have been developed to control this interaction, using assemblies of nanostructures that interact electromagnetically among them and in some case use their resonant nature[1]. A metamaterial is a material that has properties that go beyond the simple mixing of its components. The key point is that metamaterials attain their properties from the unit structure rather than the constituent materials. Usually, these composites are called *"meta-structures"*, since they essentially recreate the atomic-like structure of matter at the nanoscale. In general, the components of metamaterials must be smaller than the wavelength of interest, producing an inhomogeneity at this level. Furthermore, the lattice parameter of the nanostructure must also be subwavelength in scale. The microscopic inhomogeneity in a metamaterial makes the whole material macroscopically uniform avoiding the diffraction and interference phenomena,

[1] Metamaterials has become a field of its own, and there are thousands of publications, for which is much better to look up directly in the www for the specific topic, instead of giving particular references

and the description of its electromagnetic response is given in terms of macroscopic or homogenized material parameters such as the electric permittivity or the magnetic permeability. [4]

The arrival of structured metamaterials has allowed for the design of new materials, with an unprecedented amount of control over their intrinsic properties. [5] Since the dimensions, shape, as well as nature of its constituents, can be controlled, tailoring, and customized to exhibit specific phenomena in different ranges of the electromagnetic spectrum, the determined design of nanostructures will define the interaction of the materials with light, producing a wide variation in the spectral response and functionalities, and allowing the exploration of several novel phenomena, most of which cannot be found in nature. [6] The theoretical exploration has been possible due to the progress in theory of nanostructures, the wide spread use of computational tools, and numerical methods to simulate and design these new and unprecedented materials. However, the study of metamaterials is not limited to theoretical analysis of materials or the predictions of new properties; it is desired to have minimal conditions for their materialization. In this sense, the rapid advances in nano-fabrication technology during the last years, [7] and the development of a plentiful of nano-fabrication techniques have allowed the manufacture of most of these metamaterials. [8] Some of those techniques include electron-beam lithography, [9] focused ion beam milling, [10] nanoimprint lithography, [11] interference optical lithography, and nanosphere lithography. [12] All of these factor have contributed to the huge impact of metamaterials in various areas of science, technology, and engineering with a plethora of applications and potential developments. [13]

Initially, the research on metamaterials was motivated by the seminal work of Veselago in 1968 [14], and in 2000 Pendry [15], where they discussed about the possibility of the construction of materials with a negative refractive index. The capability to

fabricate this kind of metamaterials was demonstrated by Smith in 2000 [16], with the fabrication of a metamaterial based on a periodic array of metallic split-ring resonators within a dielectric matrix, that exhibited a negative refractive index. These metamaterials typically are named *"left-handed metamaterials"*, and they were the detonators in the development of perfect lenses. Nowadays, metamaterials has become a multidisciplinary field of optics. It has produced the emerging of multiple key research directions, such as optical magnetism, optical negative-index materials, giant artificial chirality, super-resolution with metamaterials, and electromagnetic cloaks of invisibility. Furthermore, metamaterials have played a crucial role in super- and hyper-lenses for high-resolution imaging, sensing and filtering, signal processing, and for the development of miniature antennae, novel waveguides, nanoscale photolithography and photonic circuits. A wide variety of applications using metamaterials have now been developed. Materials can be designed to have a negative index of refraction [17]; this has been implemented using periodic noble metal inclusions within a dielectric matrix [18]. Flat lens-like devices can be fabricated using metamaterials that can manipulate the propagation of light with sub-wavelength focusing capabilities; [15] this type of device has been implemented for cloaking [19–21] and shielding applications [22]. The fabrication of these materials is not restricted to any range in the electromagnetic spectrum, which allows for the development of new devices designed to work in the terahertz regime [23–25]. Such a feature has made it possible to design active metamaterial devices with various tunable functionalities such as switching and filtering. At microwave frequencies, such reconfigurable metamaterials can be achieved by introducing power-dependent lumped elements such as varactor diodes. Several microwave metamaterials based on varactor devices have been experimentally reported, ranging from tunable split ring resonators (SRRs) as notch filters to Second-Harmonic Generation in transmission-line NIMs. Thus, we note the significance of nanophotonics in our days. It has become in one of the most impor-

tant branch of the optics and photonics sciences, providing a novel way to study and develop new materials for future applications.

1.2 Optical Non-Linear Metamaterials

As previously stated, metamaterials display a wide variation of optical phenomena. This variety includes the nonlinear response of metamaterials, which is very important in different branches of optics and photonics. [26,27] In conventional materials, the presence of nonlinear effects strongly depends on the intrinsic nonlinear susceptibility or the intensity of the applied electric field. Furthermore, in macroscopic bulk crystals, the natural atomic structure plays a primordial role, since nonlinear phenomena are heavily sensitive to that feature, allowing or forbidding the generation of specific effects. For example, for second harmonic generation (SHG), a second-order phenomenon, the material must have a non-centrosymmetric crystalline structure to show an intense dipolar nonlinear response. On the other hand, third-order phenomena as third-harmonic generation (THG), does imposes any symmetry condition to the crystalline structure to exhibit a nonlinear optical response. Metamaterials besides can take advantage of the physical features in their nanostructure and the local environment of each component, allowing the presence of nonlinear effects at nanoscale. [28, 29] In this way, nonlinear optics has benefited from research into nonlinear metamaterials; using of metamaterials in nonlinear experiments avoids the use of extreme intensities of the electric field that could be detrimental for most of the nonlinear crystals. [30] It is critical to acquire flexible control over the characteristics of nanostructures in order to achieve the necessary functionality. The capacity to create these tailored nonlinear materials opens new possibilities for research on nonlinear light-matter interactions at subwavelength scales, promising many potential applications, for example: the design of nonlinear

nanoantennas, light sources, nanophotonic circuits for nanoscale electronics, biosensing, nano-lasers, and ultrafast miniature metadevices.

The rapid progress in the study of nonlinear properties of metamaterials has resulted in the meaningful development of new materials able to achieve nonlinear effects. Although SHG and THG have received a lot of attention, nonlinear optics in metamaterials is not just about those two phenomena. Novel structures have been developed to show other important nonlinear effects, such as three and four-wave mixing effects (TWM and FWM), the optical Kerr effect, optical parametric amplification (OPA), self-phase modulation (SPM), super continuum generation, and stimulated Raman scattering (SRS), to mention a few. There have been numerous theoretical [31–33] and experimental [22, 34, 35] studies concerning the development of nonlinear devices using metamaterials. Some examples of nonlinear metamaterials have been fabricated using split-ring resonators [36, 37] and nano-rod inclusions [38], producing SHG-active, magnetic, and left-handed materials. Other inclusions can be intrinsically noncentrosymmetric [39], thus creating a strong SHG response. Tailored metamaterials allow for the possibility to tune the nonlinear optical response [40–43] as a function of the geometrical configuration.

Nanophotonic devices are normally fabricated in the form of diverse types of structures from metallic, metal-dielectric, and all dielectric materials. In this case the improvement of the nonlinear optical effects is because of the tight confinement of the local electromagnetic fields present in subwavelength nanostructures, and the efficiency is influenced by the strong light-matter interaction and large enhancement of effective nonlinearities of the nanostructure. [44] In this way metamaterials can be designed using metallic surfaces and nanoparticles, periodic noble metal inclusions within a dielectric matrix [18], or a specific combination of them. Most of the attention has been paid to this type of metamaterials, where the free-carrier oscillations are very important.

In a metallic structure or dielectric metal interfaces, exist delocalization and coherent oscillations of the free electrons at the interface of the components, known as surface plasmon resonances (SPRs). [45] In general, they are classified in two different cases: surface plasmon polaritons (SPPs), and localized surface plasmon resonances (LSPRs). SPPs are considered propagating waves along the metal-dielectric interface, whereas LSPRs are non propagated modes localized at the surface of the nanoparticle or nanostructure. Specifically, LSPR are associate to oscillations in confined geometries; they induce a high enhancement of local field, that is expressed as strong localized intensities in the electric field, commonly observed as "hotspots" in gap regions of nanoantennas or dimmer nanostructures. These resonances have particular intensity and take place at specific frequencies, which are determined by the size, shape, and characteristic geometry of the nanostructure, or particles. For example, gold and silver nanoparticles have distinct and adjustable optical characteristics at visible frequencies, giving them a bright coloration. Also, non-resonant geometric effects lead to other optical phenomena in the interaction of light and plasmonic structures, such as scattering, absorption, as well as various nonlinear optical process, including harmonic generation. Furthermore, *lightning rod* effects on sharp nanoscale tips and edges can appear. All these mechanisms provide an extreme enhancement of the electric fields, making plasmonics a powerful tool for nonlinear optics. It opens the possibility for very high field magnitudes in small volumes, allowing strong nonlinear enhancement at the nanoscale.

Various nonlinear optical processes, such as SHG, multiphoton excited luminescence, third-harmonic generation(THG), or four-wave mixing (FWM), have been observed in plasmonic nanostructures, highlighting their tremendous potential for designing advanced nonlinear nano-sources of light and manipulating light at small scales. Enhanced harmonic generation has been seen in a variety of structures, including nano-cones, nanoscale apertures and dimers, nano-cups, tapered waveguides, and more. Dimer nano

antennas, pairs of metallic cylinders or bars separated by a small gap, typically show strong field enhancement in the gap, which can be exploited for the study of second and third harmonic generation. Four-wave mixing (FWM) has also been reported on nanostructured surfaces. The combination of the strong near-field intensity obtained with plasmonic systems and the intrinsic nonlinearities of metals readily results in efficient nonlinear optical processes, which have given rise to the new research field of nonlinear plasmonic.

SHG is one of the most common nonlinear optical phenomena investigated due to the wide range of applications it offers; it was first observed by Franken et al. in 1961 [46]. Over the years, many theoretical models and calculations have been reported to explore SH radiation (scattered and reflected, coherent and incoherent) and the efficiency of the conversion process. SHG had taken the benefits of plasmonic effects all of previous conditions are outstanding to achieve that phenomena; it has been observed that for centrosymmetric nanostructures, the influence of strong absorption is fundamental to attain a great efficiency in the nonlinear process, besides that the peak on SHG signal is located at peak of linear absorption. In particular, SHG from metasurfaces, nanoparticles and nanostructures has been extensively studied experimentally and by diverse numerical methods such as the finite difference in the time domain method (FDTD), [47] the surface integral equation (SIE) method, the finite element (FEM) technique and the discrete dipole approximation (DDA). [47, 48]

A wide variety of applications using metamaterials have now been developed. Materials can be designed to have a negative index of refraction [17]; this has been implemented using periodic noble metal inclusions within a dielectric matrix [18]. Flat lens-like devices can be fabricated using metamaterials that can manipulate the propagation of light with sub-wavelength focusing capabilities; [15] this type of device has been implemented for cloaking [19–21] and shielding applications [22]. The fabrica-

tion of these materials is not restricted to any range in the electromagnetic spectrum, which allows for the development of new devices designed to work in the terahertz regime [23–25].

The required physical parameters (namely, the electric permittivity and magnetic permeability) that are used for calculating the optical response can be obtained via the homogenization of the electric field [16, 49, 50]. These parameters are also used in the experimental characterization of the metamaterials studied in this thesis. The formalism presented in Refs. [51] and [52] is used in this work to describe the macroscopic response of inhomogeneous systems as an average of the microscopic response of the system. These quantities can then be used to calculate the linear and non-linear optical responses of a given metamaterial of arbitrary composition [53–57].

1.3 Scope of the Thesis

In this thesis, we explore the nonlinear SH response of a periodic nanostructured metamaterial comprised of a bulk silver matrix with vacuum inclusions. We mention that the theoretical approach of this thesis is based on Haydock's approach which makes it unique in this respect and thus there are no other articles using this novel technique, that also includes our own numerical implementation in the PHOTONIC software. [58] We change the macroscopic structure by varying various geometrical parameters in order to produce, enhance, and vary the SH signal. We systematically study the evolution of the nonlinear susceptibility tensor due to variations in the shape and position of the inclusions in the metamaterial. These variations can significantly alter the centrosymmetry of the material, causing changes in both the position and the intensity of the SHG resonances. Lastly, we elucidate the origin of the produced SH response by calculating and analyzing the charge density and polarization field at the metallic surface.

1.4 Thesis Outline

The thesis is divided into 4 chapters including this introduction. In Chapter 2, using the *dipollium* model, we investigate the SHG of nano-structured metamaterials, showing that by controlling the non-centrosymmetry of the structure SHG can be readily manipulated. We do so by using a silver T-shape nanostructure and the homogenization method in order to calculate the effective properties in metamaterials, as well as the implementation of Haydock's recursive method. In Chapter 3, we present results for linear response for a variety of three different geometries; gold nano-prisms and U-shaped gold rectangular Split Ring Resonators. Finally, in Chapter 4 we present our final observations, remarks and perspectives for future work. Appendix A presents remarkable details in the homogenization procedure and its connection with the Haydock recursive method. Appendix B presents the complete, step-by-step derivations for the SSHG yield. In Appendix C, we show the main achievements of this work in terms of published articles and attended conferences. Finally, the complete bibliography is located at the end of the document for easy reference.

2 Second Harmonic Generation in Nano-structured Metamaterials

In this chapter we develop a method to calculate the Second Harmonic Generation (SHG) of nano-structured metamaterials based on a novel solution of Maxwell's equations through the Haydock recursion scheme. [59] The content of this chapter is based on the article "Second-harmonic generation in nanostructured metamaterials" published in Physical Review B, **99** (12), 2019, whose authors are Ulises R. Meza, Bernardo S. Mendoza, and W. Luis Mochán. [60] This article is part of the achievements of the present doctoral thesis as cited in App. C.

2.1 Introduction

The advent of structured metamaterials has allowed the design of new materials, with an unprecedented amount of control over their intrinsic properties. These metamaterials are typically composite systems that consist of two or more ordinary materials, that are periodically structured or arranged in such a manner that the resulting prop-

erties differ from those of the constituent materials. These systems have been widely explored both theoretically and experimentally, with a plethora of new applications under development [14, 16, 31, 35, 61, 62]. The variety of available fabrication techniques such as electron-beam lithography [63–65], ion milling [66, 67], and even conventional 3D printing [68–70], allow for extremely precise designs of structured systems featuring arrays of inclusions (or holes) with specific shapes. These methods allow the possibility to fabricate new devices with highly tunable optoelectronic properties [15, 16]. A wide variety of applications using metamaterials have now been developed. Materials can be designed to have a negative index of refraction [17]; this has been implemented using periodic noble metal inclusions within a dielectric matrix [18]. Flat lens-like devices can be fabricated using metamaterials that can manipulate the propagation of light with sub-wavelength focusing capabilities; [15] this type of device has been implemented for cloaking [19–21] and shielding applications [22]. The fabrication of these materials is not restricted to specific ranges of the electromagnetic spectrum, which allows for the development of new devices designed to work in the terahertz regime [23–25].

Metamaterials display a wide variety of optical phenomena [71]; of particular interest to us are their nonlinear optical properties. The nonlinear response is strongly sensitive to the natural atomic structure; for second-harmonic generation (SHG), the material must have a non-centrosymmetric crystalline structure in order to have a strong dipolar nonlinear response. Structured metamaterials, that can be designed with almost limitless configurations, make for a promising alternative for nonlinear optical applications. There have been numerous theoretical [31–33] and experimental [22, 34, 35] studies concerning the development of nonlinear devices using metamaterials. Some examples of nonlinear metamaterials have been fabricated using split-ring resonators [36, 37] and nano-rod inclusions [38], producing SHG-active, magnetic, and left-handed materials. Other inclusions can be intrinsically noncentrosymmetric [39], thus creating a strong

SHG response. Tailored metamaterials allow for the possibility to tune the nonlinear optical response [40–43] as a function of the geometrical configuration. Plasmonic metamaterials may further enhance the nonlinearities through the field amplification associated to plasmonic resonances. These systems can be varied geometrically, changing their degree of non-centrosymmetry, thus allowing for the second-harmonic (SH) signal to be enhanced.

An even richer set of possibilities opens up when 2D plasmonic metasurfaces are considered. These are made of arrays of structures with a sub-wavelength thickness known as meta-atoms, which permit the manipulation of the polarization, amplitude and phase of light. For example, a simple rotation of a non-centrosymmetric pseudo-atom allows a change of phase of the second harmonic field it generates, so that a metasurface whose atoms have a position dependent orientation may produce SHG beams propagating into specific angles according to its polarization. For a review of phenomena such as giant circular dichroism, nonlinear Berry phase and wavefront engineering and many others at non-linear plasmonic metasurfaces see Ref. [72]. Instead of plasmonic systems, for which dissipation may be problematic, all dielectric structures made of materials with a high index of refraction (high n) have also been proposed, where there are Mie like resonances which yield large localized field amplitudes which produce non-linear optical effects. Devices based on these resonances include controllable directional radiators due to the interference of electric and magnetic multipolar resonances, high efficiency metalenses, metasurface holograms and active nanophotonics. [73, 74] It has been shown that in metasurfaces made of non-centrosymmetric high n meta-molecules, made of pairs of slightly different meta-atoms, quasi-bound electromagnetic modes that coexist with the continuum of propagating electromagnetic waves may be excited, where the bound character arises due to the destructive interference between the far field of two modes whose frequencies display an avoided crossing as the geometric parameters of the system are

varied. In this situation, the electric field in the neighbourhood of the meta-molecule is amplified, producing non-linear effects, and in particular, very large enhancement of the SHG. [75]

The required physical parameters (namely, the electric permittivity and magnetic permeability) that are used for calculating the linear optical response can be obtained via a homogenization procedure [16,49,50]. The formalism presented in Refs. [51] and [52] is used in this work to describe the macroscopic linear response of inhomogeneous systems in terms of an average of certain specific microscopic response functions of the system. We first extend this formalism to calculate not only the linear but also the non-linear optical second order susceptibility of metamaterials of arbitrary composition [53–56] in terms of its linear response and allowing for dispersion and dissipation. We illustrate the formalism exploring the nonlinear SH response of a periodic nano-structured 2D metamaterial comprised of an array of holes of a non-centrosymmetric shape within a matrix made of a centrosymmetric material, for which we chose silver. In this case, the SH generation from a homogeneous matrix would be strongly suppressed, but the noncentrosymmetric geometry of the holes allows a strong signal whose resonances may be tuned and enhanced through variations of the geometrical parameters [76, 77]. We systematically study the evolution of the nonlinear susceptibility tensor due to variations in the shape and position of the holes. Lastly, we elucidate the origin of the produced SH response by calculating and analyzing the charge density and polarization field at the metallic surface. We have built computational packages for the calculation of the surface and bulk nonlinear polarization of nano-structured metamaterials and we have added them to the publicly available modular computational software Photonic developed by our group.

The chapter is organized as follows. In Sec. 2.2 we present the theoretical approach used to calculate the dielectric response of the metamaterial that is then used to obtain

the nonlinear SH polarization. In Sec. 2.3 we present results for a nanostructured metamaterial consisting of empty holes within a silver matrix. We explore a variety of geometric configurations to fine-tune the SH response. We mention that the work presented in this chapter is published in Ref. [60].

2.2 Theory

The quadratic polarization forced at the second-harmonic (SH) frequency 2ω by an inhomogeneous fundamental field $\boldsymbol{E}_\omega$ at frequency ω within an isotropic centrosymmetric material system made of polarizable entities within the non-retarded regime may be written as [78]

$$\boldsymbol{P}^f(2\omega) = n\boldsymbol{p}(2\omega) - \frac{1}{2}\nabla \cdot n\boldsymbol{Q}(2\omega) \tag{2.1}$$

where n is the number density of polarizable entities, $\boldsymbol{p}(2\omega)$ is their electric dipole moment and is given within the *dipolium* model [79] by

$$\boldsymbol{p}(2\omega) = -\frac{n}{2e}\alpha(\omega)\alpha(2\omega)\nabla E^2(\omega), \tag{2.2}$$

$\boldsymbol{Q}(2\omega)$ is their electric quadrupole moment, given by

$$\boldsymbol{Q}(2\omega) = \frac{1}{2e}n\alpha^2(\omega)\boldsymbol{E}(\omega)\boldsymbol{E}(\omega), \tag{2.3}$$

and $\alpha(\nu\omega)$ are the the linear polarizabilities of each entity at the fundamental ($\nu = 1$) and at the SH ($\nu = 2$), related to the dielectric function $\epsilon(\nu\omega)$ through

$$\epsilon(\nu\omega) = 1 + 4\pi n\alpha(\nu\omega). \tag{2.4}$$

The non-linear current density may be obtained from the polarization through $\boldsymbol{j}^f = \partial\boldsymbol{P}^f/\partial t$. We could expect an additional contribution $c\boldsymbol{\nabla} \times \boldsymbol{M}^f$ from a magnetization $\boldsymbol{M}^f = n\boldsymbol{m}$, with $\boldsymbol{m}$ the second order magnetic dipole moment for each polarizable

entity. However, within the dipolium model the quadratic magnetic dipole induced in each polarizable entity is null for SHG. [80–82]

We allow the density n, the polarizability α, the dielectric response ϵ and the field to depend on position. The total polarization induced at the SH is then

$$\begin{aligned}\boldsymbol{P}(2\omega) =& n\alpha(2\omega)\boldsymbol{E}(2\omega) + \boldsymbol{P}^f(2\omega) && (2.5)\\ =& n\alpha(2\omega)\boldsymbol{E}(2\omega) - \frac{n}{2e}\alpha(\omega)\alpha(2\omega)\nabla E^2(\omega) && (2.6)\\ &+ \frac{1}{2e}\nabla\cdot n\alpha^2(\omega)\boldsymbol{E}(\omega)\boldsymbol{E}(\omega), && (2.7)\end{aligned}$$

where we added to Eq. (2.1) the polarization linearly induced by the electric field $\boldsymbol{E}(2\omega)$ produced (self consistently) by the total polarization $\boldsymbol{P}(2\omega)$.

The equations above were developed for an insulating material, for which the polarizable entities are atoms whose electronic dynamics are described by harmonic forces, but by writing the linear polarizability at the fundamental and second harmonic frequencies in terms of the dielectric function of the material, they can be applied to arbitrary insulators or semiconductors. An alternative model for the description of metals starts from the Euler hydrodynamic equation for their conduction electrons,

$$nm\left(\frac{\partial}{\partial t}\boldsymbol{v} + \boldsymbol{v}\cdot\boldsymbol{\nabla}\boldsymbol{v} + \frac{\boldsymbol{v}}{\tau}\right) = -en\boldsymbol{E} - ne\frac{\boldsymbol{v}}{c}\times\boldsymbol{B} \tag{2.8}$$

where $n, \boldsymbol{v}$, and τ are the electronic density, velocity and lifetime respectively, and in which the non-linearity arises from the magnetic interaction and the convective contribution to the time derivative. It has been shown that this model yields the same result as the dipolium model when we identify $\boldsymbol{j} = -ne\boldsymbol{v}$ with the time derivative of the polarization $\boldsymbol{j} = \partial\boldsymbol{P}/\partial t$ and write the resulting response in terms of the linear dielectric function [80]. Thus, Eq.(2.5) describes the contributions of both, bound and free electrons to the nonlinear polarization and can be used for metallic as well as dielectric systems.

We want to apply the equations above to obtain the nonlinear susceptibility of a binary metamaterial consisting of two phases: a host made up some material A in which inclusions made up of a material B are embedded forming a periodic lattice. In our actual calculations we will replace material B by vacuum. We denote by ϵ_γ, α_γ and n_γ the dielectric function, polarizability and number density corresponding to material $\gamma = A,\ B$. We may describe the geometry of the metamaterial through a periodic *characteristic function* $B(\boldsymbol{r}) = B(\boldsymbol{r} + \boldsymbol{R})$ which takes the values 1 or 0, according to whether the position $\boldsymbol{r}$ lies within the region occupied by material B or A, respectively, and where $\boldsymbol{R}$ is a lattice vector. Thus, we may write the dielectric function as

$$\epsilon(\boldsymbol{r}) = \frac{\epsilon_A}{u}(u - B(\boldsymbol{r})), \tag{2.9}$$

where we introduced the spectral variable

$$u = \frac{1}{1 - \epsilon_B/\epsilon_A}, \tag{2.10}$$

which takes complex values in general and accounts for the composition of the materials and for their frequency dependent response.

In the long-wavelength approximation, assuming that the unit cell of the metamaterial is small compared to the wavelength of light in vacuum and the wave- or decay-length within each of its components, the spatial fluctuations of the electric field are longitudinal [51] and the transverse or longitudinal nature of macroscopic field is irrelevant, so we may take the electric field within a single cell as longitudinal $\boldsymbol{E} = \boldsymbol{E}^L$ and we may identify the longitudinal part $\boldsymbol{D}^L$ of the displacement field $\boldsymbol{D}$ as an *external* field, which therefore has no fluctuations originated in the spatial texture of the metamaterial, and is thus a macroscopic field $\boldsymbol{D}^L = \boldsymbol{D}^L_M$. Then, if we excite the system with a longitudinal external field we may write

$$\boldsymbol{E} = (\hat{\boldsymbol{\epsilon}}^{LL})^{-1}\boldsymbol{D}^L, \tag{2.11}$$

and

$$\boldsymbol{E}_M = (\hat{\boldsymbol{\epsilon}}_M^{LL})^{-1}\boldsymbol{D}_M^L, \tag{2.12}$$

where $\hat{\boldsymbol{\epsilon}}^{LL} = \hat{\mathcal{P}}^L\hat{\epsilon}\hat{\mathcal{P}}^L$ is the longitudinal projection of the dielectric function ϵ interpreted as a linear operator,

$$(\hat{\boldsymbol{\epsilon}}_M^{LL})^{-1} = \left\langle(\hat{\boldsymbol{\epsilon}}^{LL})^{-1}\right\rangle, \tag{2.13}$$

is the inverse of the macroscopic longitudinal dielectric operator, given by the spatial average [51,52] $\langle\ldots\rangle$, of the *microscopic* inverse longitudinal dielectric operator, and $\hat{\mathcal{P}}^L$ is the longitudinal projector operator, which may be represented in reciprocal space by the matrix

$$\mathcal{P}_{\boldsymbol{GG'}} = \hat{\boldsymbol{G}}\hat{\boldsymbol{G}}\delta_{\boldsymbol{GG'}}, \tag{2.14}$$

where $\boldsymbol{G}$ and $\boldsymbol{G'}$ are reciprocal vectors of the metamaterial, $\delta_{\boldsymbol{GG'}}$ is Kronecker's delta,

$$\hat{\boldsymbol{G}} = \frac{\boldsymbol{k}+\boldsymbol{G}}{||\boldsymbol{k}+\boldsymbol{G}||} \tag{2.15}$$

is a unit vector in the direction of the wavevector $\boldsymbol{k}+\boldsymbol{G}$, and $\boldsymbol{k}$ the conserved Bloch's vector of the linear field which we interpret as the relatively small wavevector of the macroscopic field.

From Eq. (2.9) we may write

$$(\hat{\boldsymbol{\epsilon}}^{LL})^{-1} = \frac{u}{\epsilon_A}(u\hat{\mathcal{P}}^L - \hat{B}^{LL})^{-1}, \tag{2.16}$$

in which we may interpret the inverse of the operator within parenthesis in terms of a Green's function,

$$\hat{\mathcal{G}}(u) = (u-\hat{\mathcal{H}})^{-1}, \tag{2.17}$$

the resolvent of a Hermitian operator $\hat{\mathcal{H}}$ with matrix elements

$$\mathcal{H}_{\boldsymbol{GG'}} = \hat{\boldsymbol{G}}\cdot B(\boldsymbol{G}-\boldsymbol{G'})\hat{\boldsymbol{G}'} \tag{2.18}$$

in reciprocal space, where $B(\boldsymbol{G}-\boldsymbol{G}')$ is the Fourier coefficient of the periodic characteristic function $B(\boldsymbol{r})$ with wavevector $(\boldsymbol{G}-\boldsymbol{G}')$. Notice that $B^{LL}_{\boldsymbol{G}\boldsymbol{G}'} = \hat{\boldsymbol{G}}\mathcal{H}_{\boldsymbol{G}\boldsymbol{G}'}\hat{\boldsymbol{G}}'$, $(\boldsymbol{\epsilon}^{LL})^{-1}_{\boldsymbol{G}\boldsymbol{G}'} = (u/\epsilon_A)\hat{\boldsymbol{G}}\hat{\mathcal{G}}(u)\hat{\boldsymbol{G}}'$, and that $(\boldsymbol{\epsilon}^{LL}_M)^{-1} = (u/\epsilon_A)\hat{\boldsymbol{k}}\langle\hat{\mathcal{G}}(u)\rangle\hat{\boldsymbol{k}}$.

To obtain the macroscopic dielectric response and the microscopic electric field we proceed as follows. We define a normalized macroscopic state $|0\rangle$ that represents a longitudinal field propagating with the given small wavevector $\boldsymbol{k}$ and we act repeatedly on this state with the operator $\hat{\mathcal{H}}$ to generate an orthonormal basis set $\{|n\rangle\}$ through Haydock's [59] recursion

$$\hat{\mathcal{H}}|n\rangle = b_{n+1}|n+1\rangle + a_n|n\rangle + b_n|n-1\rangle. \tag{2.19}$$

In this basis, $\hat{\mathcal{H}}$ may be represented by a tridiagonal matrix with elements

$$(\mathcal{H}_{nn'}) = \begin{pmatrix} a_0 & b_1 & 0 & 0 & \cdots \\ b_1 & a_1 & b_2 & 0 & \cdots \\ 0 & b_2 & a_2 & b_3 & \cdots \\ 0 & 0 & b_3 & a_3 & \cdots \\ \vdots & \vdots & \vdots & \vdots & \ddots \end{pmatrix} \tag{2.20}$$

given by Haydock's coefficients a_n and b_n. Thus, the macroscopic inverse longitudinal response may be obtained as a continued fraction [54, 55]

$$\begin{aligned}(\hat{\boldsymbol{\epsilon}}^{LL}_M)^{-1} &= \hat{\boldsymbol{k}}\hat{\boldsymbol{k}}\frac{u}{\epsilon_A}\langle 0|(u-\hat{H})^{-1}|0\rangle \\ &= \hat{\boldsymbol{k}}\hat{\boldsymbol{k}}\frac{u}{\epsilon_A}\cfrac{1}{u-a_0-\cfrac{b_1^2}{u-a_1-\cfrac{b_2^2}{u-a_2-\cfrac{b_3^2}{\ddots}}}}\end{aligned} \tag{2.21}$$

and the microscopic electric field (2.11) may be represented in reciprocal space by

$$E_G = \sum \zeta_n \langle \boldsymbol{G}|n\rangle \tag{2.22}$$

with coefficients ζ_n obtained by solving the tridiagonal system

$$\sum_{n'}(u\delta_{nn'} - H_{nn'})\zeta_{n'} = \delta_{n0}D^L, \tag{2.23}$$

where we write the fields in real space as

$$\boldsymbol{D}^L(\boldsymbol{r}) = \hat{\boldsymbol{k}}D^L e^{i\boldsymbol{k}\cdot\boldsymbol{r}} \tag{2.24}$$

and

$$\boldsymbol{E}(\boldsymbol{r}) = \sum_{\boldsymbol{G}} \hat{\boldsymbol{G}}E_G e^{i(\boldsymbol{k}+\boldsymbol{G})\cdot\boldsymbol{r}}. \tag{2.25}$$

Notice that the results of the calculation above depend on the direction $\hat{\boldsymbol{k}}$ chosen as the propagation direction of the external field. As we may identify

$$(\hat{\boldsymbol{\epsilon}}_M^{LL})^{-1} = \frac{\hat{\boldsymbol{k}}\hat{\boldsymbol{k}}}{\hat{\boldsymbol{k}}.\hat{\boldsymbol{\epsilon}}_M^{LL}\cdot\hat{\boldsymbol{k}}}, \tag{2.26}$$

all the components of the macroscopic dielectric tensor may be efficiently obtained from Eq. (2.21) by repeating the calculation of its longitudinal projection for different propagation directions $\hat{\boldsymbol{k}}$, such as along all independent combinations $\hat{\boldsymbol{e}}_i + \hat{\boldsymbol{e}}_j$ of pairs of Cartesian directions $\hat{\boldsymbol{e}}_i$ and $\hat{\boldsymbol{e}}_j$ ($i, j = x$, y or z).

We remark that the small-scale fluctuations of the electric field within a nano-structured system within the long-wavelength regime are mostly longitudinal, as the transverse contributions are of an order a^2/λ^2 smaller (45,46), where a is the lattice parameter and λ the free-space wavelength. On the other hand, the macroscopic field is almost constant within the small unit cell, so its transverse or longitudinal character is irrelevant. For these reasons, after having identified all of the components of the dielectric tensor, the results above are suitable for the common case of electromagnetic waves for which the macroscopic field is actually transverse, not longitudinal. These remarks have been verified by comparing the full numerical solution of the wave equation within a metamaterial with the efficient solution proposed above [53, 83]

2.3 Non-linear Susceptibility $\chi^{(2)}$

Once we obtain the microscopic field from Eqs. (2.22), (2.23) and (2.25), we may substitute it in Eqs. (2.1)-(2.3) to obtain the forced SH polarization, which we may then substitute in Eq. (2.5) to obtain the self consistent quadratic polarization in the SH. However, in order to solve Eq. (2.5) we need the selfconsistent SH field, which in the long wavelength approximation is simply given by the depolarization field

$$\boldsymbol{E}(2\omega) = -4\pi \boldsymbol{P}^L(2\omega) \tag{2.27}$$

produced only by the longitudinal part of the SH polarization. Thus we write Eq. (2.5) as

$$\boldsymbol{P}(2\omega) = -4\pi n\alpha(2\omega)\boldsymbol{P}^L(2\omega) + \boldsymbol{P}^f(2\omega). \tag{2.28}$$

By taking the longitudinal projection we obtain a closed equation for $\boldsymbol{P}^L(2\omega)$ which we solve formally as

$$\boldsymbol{P}^L(2\omega) = (\hat{\boldsymbol{\epsilon}}^{LL}(2\omega))^{-1}\boldsymbol{P}^{fL}(2\omega) \tag{2.29}$$

using Eq. (2.4). Plugging this result back into Eq. (2.28), we finally obtain the SH polarization $\boldsymbol{P}(2\omega)$.

In order to perform the operation indicated in Eq. (2.29) we perform a Haydock recursion as in Eq. (2.19) but using $\boldsymbol{P}^{fL}(2\omega)$ to construct a new initial normalized state $|\tilde{0}\rangle$, with components $\langle \boldsymbol{G}|\tilde{0}\rangle$ in reciprocal given by

$$\boldsymbol{P}^{fL}_{\boldsymbol{G}}(2\omega) = \hat{\boldsymbol{G}}\langle \boldsymbol{G}|\tilde{0}\rangle f, \tag{2.30}$$

where f is a normalization constant, and from it, a new Haydock orthonormal basis $|\tilde{n}\rangle$ using the same procedure as in Eq. (2.19). Thus, we write the self consistent longitudinal SH polarization as

$$\boldsymbol{P}^L(2\omega;\boldsymbol{r}) = \sum_{\boldsymbol{G}} P^L_{\boldsymbol{G}}(2\omega)\hat{\boldsymbol{G}}e^{i(\boldsymbol{k}+\boldsymbol{G})\cdot\boldsymbol{r}}. \tag{2.31}$$

with

$$P^L_{\boldsymbol{G}}(2\omega) = \frac{u_2}{\epsilon_{A2}} \sum_{\tilde{n}} \xi_{\tilde{n}} \langle \boldsymbol{G}|\tilde{n}\rangle \tag{2.32}$$

and with coefficients $\xi_{\tilde{n}}$ obtained by solving the tridiagonal system

$$\sum_{\tilde{n}'} (u_2 \delta_{\tilde{n}\tilde{n}'} - H_{\tilde{n}\tilde{n}'}) \xi_{\tilde{n}'} = \delta_{\tilde{n}\tilde{0}} f, \tag{2.33}$$

where u_2 and ϵ_{A2} are the spectral variable (2.10) and the dielectric response ϵ_A but evaluated at the SH frequency 2ω.

Substitution of $\xi_{\tilde{n}}$ from Eq. (2.33) into Eqs. (2.32) and (2.31) yields the SH longitudinal polarization, which may then be substituted into Eq. (2.28) to obtain the total SH polarization in the long-wavelength limit when the system is excited by a longitudinal external field along $\hat{\boldsymbol{k}}$. Averaging the result, or equivalently, taking the $\boldsymbol{G} = 0$ contribution in reciprocal space, we obtain the macroscopic SH polarization $\boldsymbol{P}_M(2\omega)$. Notice that we may not obtain yet the non-linear quadratic susceptibility from this polarization, as it contains a contribution from the linear response to the second harmonic electric field. Thus, we write

$$\boldsymbol{P}_M(2\omega) = \frac{1}{4\pi}(\boldsymbol{\epsilon}_M(2\omega) - \mathbf{1})\boldsymbol{E}_M(2\omega) + \boldsymbol{P}^f_M(2\omega), \tag{2.34}$$

where the first term is the contribution of the linear response to the SH macroscopic field, and the second term

$$\boldsymbol{P}^f_M(2\omega) = \boldsymbol{\chi}^{(2)}_M : \boldsymbol{E}_M(2\omega)\boldsymbol{E}_M(2\omega) \tag{2.35}$$

is the sought after SH macroscopic polarization forced by the SH macroscopic electric field, and $\boldsymbol{\chi}^{(2)}_M$ is the corresponding SH quadratic macroscopic susceptibility, given by a third rank tensor. Within our long-wavelength longitudinal calculation the macroscopic field $\boldsymbol{E}_M(2\omega)$ is simply given by the longitudinal depolarization field

$$\boldsymbol{E}_M(2\omega) = \boldsymbol{E}^L_M(2\omega) = -4\pi \boldsymbol{P}^L_M(2\omega), \tag{2.36}$$

so that, taking the longitudinal projection of Eq. (2.34) we obtain

$$\boldsymbol{P}_M^{fL}(2\omega) = \hat{\boldsymbol{k}}\hat{\boldsymbol{k}} \cdot \boldsymbol{P}_M^{f}(2\omega) = \boldsymbol{\epsilon}_M^{LL}(2\omega)\boldsymbol{P}_M^{L}(2\omega). \tag{2.37}$$

Substituting $\boldsymbol{P}_M^{fL}(2\omega)$ from Eq. (2.37) into (2.36) and then into (2.34) we obtain the macroscopic forced quadratic SH polarization $\boldsymbol{P}_M^{f}(2\omega)$ produced by a longitudinal external $\boldsymbol{D}^L$ field pointing along $\hat{\boldsymbol{k}}$. As in the linear case, we finally repeat the calculation above, for several independent directions of propagation $\hat{\boldsymbol{k}}$ so that the corresponding Eqs. (2.35) become a system of linear equations in the unknown Cartesian components $\chi^{(2)}_{M\,ijk}$ ($i, j, k = x$, y, or z) which we solve to obtain the third rank second order susceptibility tensor $\boldsymbol{\chi}_M^{(2)}$ of the metamaterial. Notice that a quadratic macroscopic electric quadrupolar density, as well as a possible quadratic macroscopic magnetic dipolar density could also produce a non-local contribution to the polarization, described by a fourth order tensor which acts on $\boldsymbol{E}_M\boldsymbol{\nabla}\boldsymbol{E}_M$. This terms would be negligible within the long-wavelength regime, except for centrosymmetric systems with a centrosymmetric geometry, for which the local contribution is suppressed.

In summary, to obtain the quadratic response we first obtain the non-retarded microscopic field and the macroscopic dielectric tensor using a Haydock's recursion starting from a macroscopic external longitudinal field, then we use the dipolium model to obtain the microscopic source of the SH polarization, which we screen using again Haydock's scheme to obtain the full microscopic polarization, which we average to obtain the full macroscopic SH polarization. As this includes a contribution from the macroscopic SH depolarization field, we subtract it before identifying the quadratic susceptibility tensor projected onto the longitudinal direction. We repeat the calculation along different independent directions so that we can extract all the components of the quadratic susceptibility.

In the process above we assumed that the unit cell of the metamaterial is small with respect to the wavelength at frequency ω, and thus we introduced a long-wavelength

approximation and assumed the external field and the electric field to be longitudinal. After obtaining all the components of the macroscopic response, we should not concern ourselves anymore with the texture of the metamaterial; the unit cell disappears from any further use we give to the macroscopic susceptibility. Thus, we can solve any macroscopic SH related electromagnetic problem using the suceptibiity obtained above without using again the long wavelength approximation. Once we have the full macroscopic susceptibility tensor we may use it to calculate the response to transverse as well as longitudinal fields. Thus, we may use our susceptibility above to study the generation of electromagnetic waves at the SH from a propagating fundamental wave, in which case the macroscopic fields should no longer be assumed to be longitudinal; it is only their spatial fluctuations, which have been homogenized away, that are necessarily longitudinal.

2.4 Results

In the present section we apply the formalism developed in the previous section to obtain the nonlinear response of a system with a simple geometry for which we can control the degree of centrosymmetry. To that end, we incorporated the scheme described in the previous section into the publicly available package *Photonic* [58], which is a modular, object oriented system based on the Perlprogramming language, its Perl Data Language (PDL) [84] extension for efficient numerical calculations, and the Moose [85] object system. The package implements Haydock's recursive procedure to calculate optical properties of structured metamaterials in the non-retarded as well as in the retarded regime.

Our system consists of a square array of pairs of holes in the shape of prisms with a rectangular cross section within a metallic host (Fig. 2.1). Each rectangle is aligned

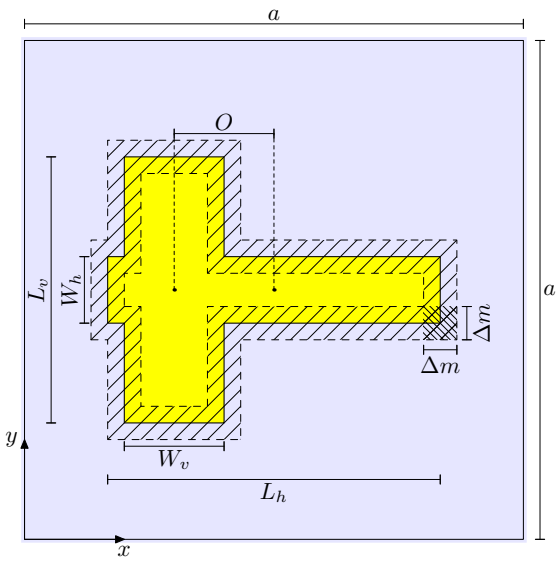

Figure 2.1: Unit cell of a metamaterial made up of a horizontal and a vertical rectangular hole within a conducting matrix. We indicate the lattice parameter a of the square array, the length L_β and width W_β of each rectangle ($\beta = h, v$) and the offset O of the vertical rectangle with respect to the center of the horizontal one. We indicate the directions x, y of the crystalline axes. The shaded regions correspond to masks of width Δm used to single out the surface and the edge contribution to the SH response

with one of the crystalline axes x, y of the metamaterial and is characterized by its length L_h or L_v and its width W_h or W_v, where h denotes horizontal (along x) and v vertical (along y) alignment. The center of the vertical rectangle is shifted horizontally with respect to the center of the horizontal rectangle by an offset O. Thus, when $O = 0$ our system is centrosymmetric and as O increases it becomes non-centrosymmetric in varying degrees.

We remark that we have chosen an essentially 2D system, assuming full translational invariance along the third dimension, as this choice allows a full analysis of the ensuing results below. Nevertheless, our formalism may also be applied to periodical binary

1D and 3D systems [54]. Furthermore, we can generalize our results to systems with an arbitrary number of phases [86] and we can apply them to finite systems such as metasurfaces.

In order to simplify our analysis, we have chosen a system that has mirror symmetry $y \leftrightarrow -y$ with respect to the center of the rectangles. Thus, the only in-plane non-null components of the SH susceptibility are [87] χ_{xxx}, χ_{xyy}, and $\chi_{yxy} = \chi_{yyx}$. We omit the sub-index M and the super-index (2) that indicate these are components of the quadratic macroscopic susceptibility in order to simplify the notation, as this yields no confusion. In Fig. 2.2 we show the spectra of the magnitude of these non-null components for an Ag host [88] and for different values of the offset O. The parameters we used were $W_h = W_v = a/6$, $L_h = L_v = a/2$, $O = 0 \ldots a/3$. Notice that when $O = 0$ the system is centrosymmetric and there is no SH signal. As O increases towards $\pm a/3$ the system becomes noncentrosymmetric. Two resonances become clearly visible and they grow in size as O increases and the system moves farther away from the centrosymmetric case. The lower energy resonance of χ_{yyx} is at a different frequency as those of χ_{xyy} and χ_{yyy} and is red shifted as the offset increases. If O increases beyond $a/3$ (not shown) the two rectangles would cease to overlap and the quadratic suceptibility would rapidly decay, until $O = a/2$ for which the system becomes exactly centrosymmetric again and the quadratic susceptibility becomes exactly null.

According to Fig. 2.2, the order of magnitude of the SH susceptibility at the resonance is around $10^2/nea$, where n is the electron density, e is the electron charge and a, as mentioned above is the lattice parameter of the square array. For typical non-centrosymmetrical materials, such as quartz, AlGaAs or LiNbO3, the corresponding order of magnitude is around $1/nea_B$, where a_B is the Bohr radius [89], which means a factor of 10^2 smaller than for the metamaterial. Thus, a centrosymmetric metallic material with a non-centrosymmetric geometry can achieve at resonance susceptibilities

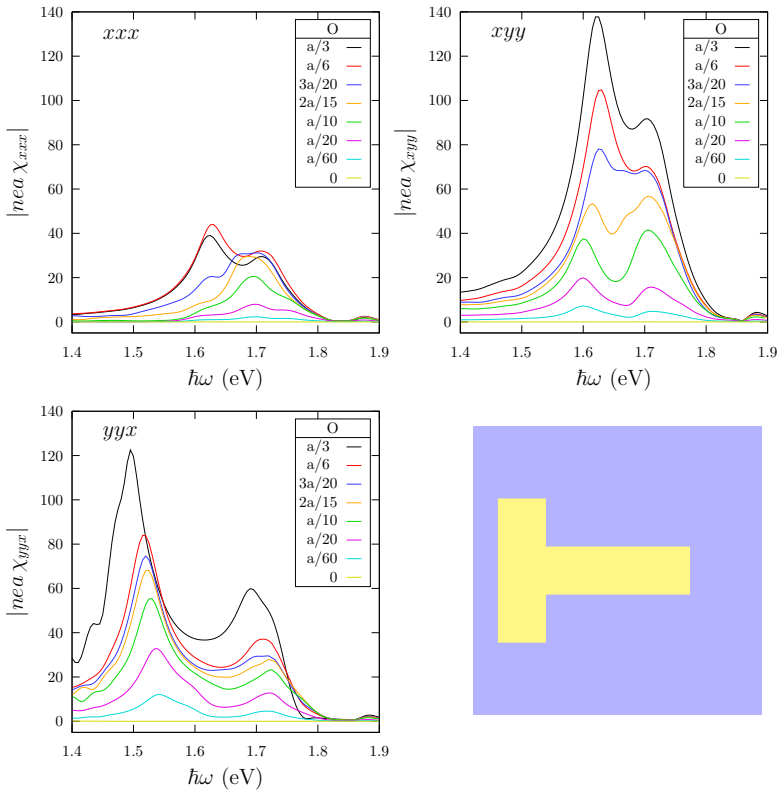

Figure 2.2: Normalized absolute value of the non-null components of the SH susceptibility $nea\chi_{ijk}$ with $ijk = xxx$ (upper left), xyy (upper right), and $yyx = yxy$ (lower left), for a square lattice of rectangular holes, as in Fig. 2.1, within Ag, with geometrical parameters $L_h = L_v = a/2$, $W_h = W_v = a/6$, for different values of the offset $O = 0 \ldots a/3$. The lower right panel displays the geometry corresponding to the largest offset. Notice that for these cases the holes overlap.

as large as $10^2 a_B/a$ times that of non-centrosymmetrical materials, even accounting for their large dissipation: for a unit cell of around 100nm this would be just one order of magnitude below those of the above mentioned systems[1].

[1]Much higher susceptibilities have been found in carefully tailored multiple quantum well structures made of noncentrosymmetric materials whose intersubband transitions where coupled to resonances of a plasmonic metasurface. See Ref. [90]

In order to understand the origin of the structure of the spectra discussed above, in Fig. 2.3 we plot the non-null components ϵ_M^{xx} and ϵ_M^{yy} of the macroscopic linear dielectric tensor $\boldsymbol{\epsilon}_M$ of a metamaterial made up of a square lattice of single rectangular holes with a horizontal orientation. Notice that there is a very weak resonance close 3.4 eV corresponding to polarization along the length of the rectangle (x direction) and a strong resonance corresponding to polarization along the width of the rectangle (y direction) at a slightly smaller frequency. Although there is a strong linear resonance in the y direction, this system is centrosymmetrical and would yield no SH signal. When we combine horizontal and vertical rectangles with a null offset $O = 0$ to make a centrosymmetric array of crosses, both resonances appear for both polarizations, although they now interact, partially exchange their strengths and repel so that both become clearly visible close to 3.4 eV and 3.2 eV (Fig. 2.4).

As the offset O (Fig. 2.1) increases there are only small changes to the spectra corresponding to ϵ_M^{xx}. However, a new mode develops in the spectra of ϵ_M^{yy}. This mode is due to the strong coupling of a quadrupolar oscillation in the vertical rectangle to the vertical dipolar oscillation of the horizontal rectangle. The quadrupole may be visualized as a horizontal polarization in the upper part of the vertical rectangle and a horizontal polarization in the opposite direction in the lower part of the rectangle, as illustrated by Fig. 2.5. The coupling is symmetry allowed as for a finite offset $O \neq 0$ the system looses the $x \leftrightarrow -x$ symmetry.

We expect the resonant structure of the quadratic susceptibility to have peaks corresponding to the resonances of the linear response at the fundamental or at the SH frequency. Thus, we expect peaks at the fundamental and at the sub-harmonics of those of the linear response. As Fig. 2.4 shows no structure at all in the the region from 1.4 eV to 1.9 eV shown in Fig. 2.2, in this case we can only expect structure at the sub-harmonics, due to a resonant excitation of the polarization at the SH frequency.

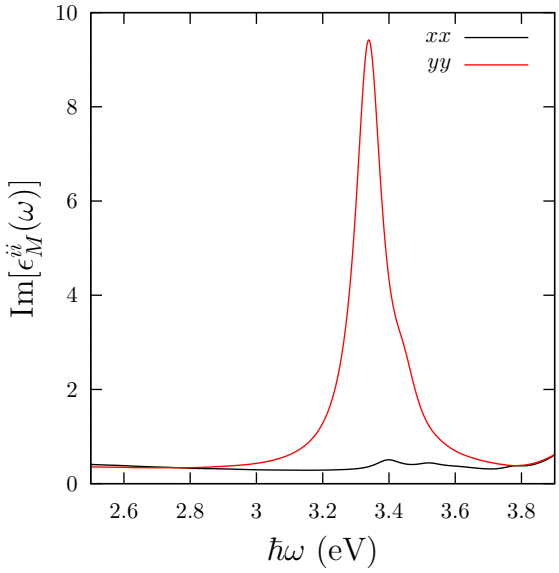

Figure 2.3: Non-null components of the macroscopic dielectric response, ϵ_M^{xx} and ϵ_M^{yy}, of a metamaterial made up of a square array of horizontally oriented single rectangular holes of length $L_h = a/2$ and width $W_h = a/6$, with a the lattice parameter within an Ag matrix.

For a macroscopic field oriented along the Cartesian directions x or y the SH harmonic polarization can only point along the x direction, due to the $y \leftrightarrow -y$ mirror symmetry of our system. Thus, the sub-harmonics of the resonances of ϵ_M^{xx} (Fig. 2.4) appear in the susceptibility components χ_{xxx} and χ_{xyy} (Fig. 2.2). On the other hand, a macroscopic field that points along an intermediate direction between x and y may excite a quadratic polarization along y. Thus, the sub-harmonics of the resonances of ϵ_M^{yy} (Fig. 2.4) appear in the susceptibility components $\chi^{yxy} = \chi^{yyx}$ (Fig. 2.2).

To gain further insight into the nature of the resonances, in Fig. 2.6 we show the polarization maps evaluated at the maxima of the SH spectra corresponding to different directions of the macroscopic linear field, and for the offset $O = a/3$ that yields the largest signals.

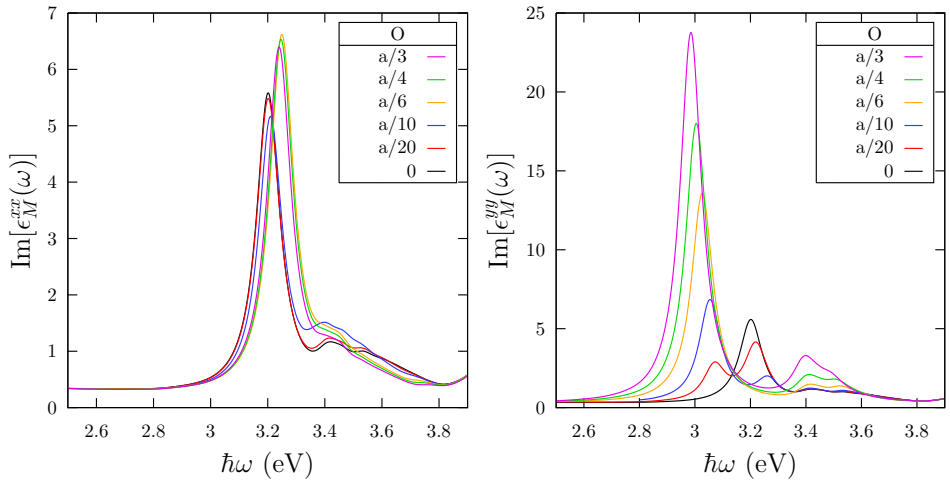

Figure 2.4: Non-null components ϵ_M^{xx} and ϵ_M^{yy} of the macroscopic dielectric tensor $\boldsymbol{\epsilon}_M$ of a metamaterial made up of a square array of pairs of horizontally and vertically oriented single rectangular holes of length $L_\beta = a/2$ and width $W_\beta = a/6$ ($\beta = h, v$), with a the lattice parameter within an Ag matrix for different values of the offset $O = 0 \ldots a/3$ (see Fig. 2.1).

We notice that when the fundamental macroscopic field points along the x direction, the magnitude of the SH polarization is symmetric with respect to the mirror plane. However, the y component of the polarization points towards opposite directions on either side of the mirror plane, yielding a macroscopic SH polarization along x. In this case, the polarization has maxima near the four concave vertices of the vertical rectangle. When the fundamental macroscopic field points along y the quadratic polarization strength is again symmetrical around the horizontal symmetry and its y component above cancels its y component below the symmetry plane, so that the resulting macroscopic SH polarization points along x. In this case, the polarization is strongest at the convex vertex where the horizontal and vertical rectangles meet, and it is slightly smaller at the other corners. On the other hand, when the fundamental macroscopic field points along the direction of $\hat{x} + \hat{y}$, the resulting quadratic polarization has no

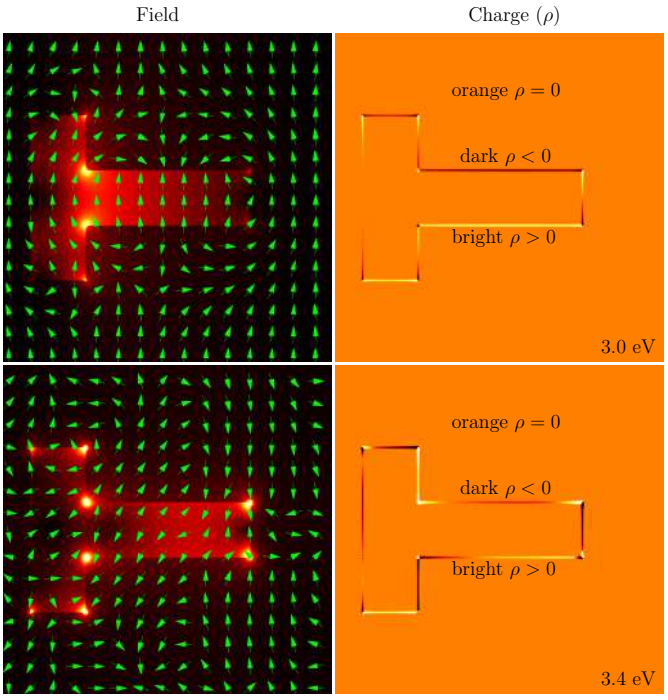

Figure 2.5: Microscopic linear electric field (left) and induced charge density ρ (right) for a metamaterial made of a square lattice of rectangular holes (Fig. 2.1 within an Ag matrix, with $L_\beta = a/2$, $W_\beta = a/6$ ($\beta = h, v$) with an offset $O = a/3$, with a the lattice parameter, excited by a macroscopic field along the y (vertical) direction with an energy $\hbar\omega \approx 3\,eV$ corresponding to the leftmost peak in ϵ_M^{yy} in Fig. 2.4. The field and the charge distribution correspond to a vertical polarization for the horizontal rectangle, a vertical polarization for the vertical rectangle and a non-diagonal quadrupole with opposite horizontal polarizations above and below the symmetry plane.

symmetry at all, and it yields a macroscopic SH polarization that has a y component.

Finally, in Fig. 2.7 we illustrate the contributions of the surface region to the total quadratic susceptibility by adding only the contributions within a band of width Δ around the surface. We notice that although there is a very strong surface polarization, its contribution to the macroscopic quadratic susceptibility is relatively small, as it is

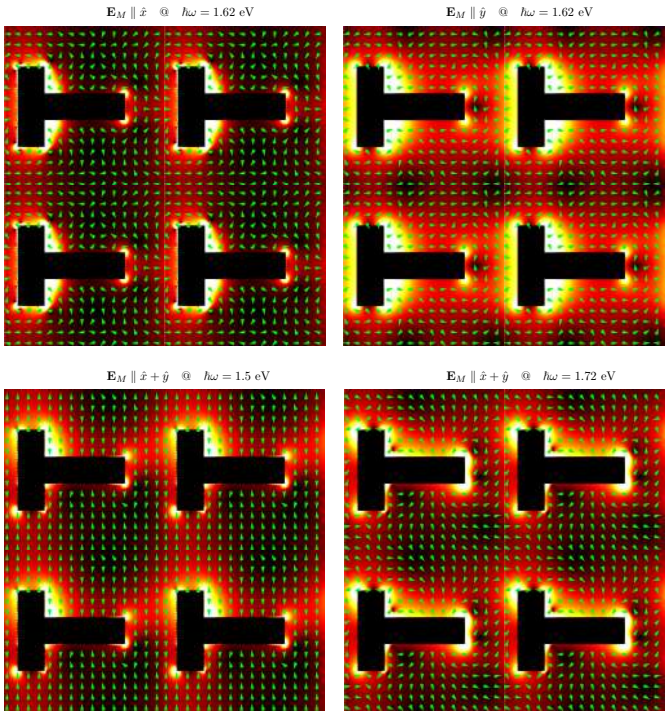

Figure 2.6: Magnitude and direction of the quadratic polarization induced in the same system as in Fig. 2.2 for the largest offset $O = a/3$ at the resonant energies $\hbar\omega = 1.72\,eV$ for the fundamental macroscopic field $\boldsymbol{E}_M$ along the direction $\hat{x} + \hat{y}$ (upper left panel), $\hbar\omega = 1.62\,eV$ and $\boldsymbol{E}_M$ along $\hat{x}$ (upper right), and for $\hbar\omega = 1.62\,eV$ and $\boldsymbol{E}_M$ along y.

confined to a very narrow region and it is partially canceled by the polarization at other parts of the surface, so that for the geometry studied here, most of the SH signal comes from the bulk of the host.

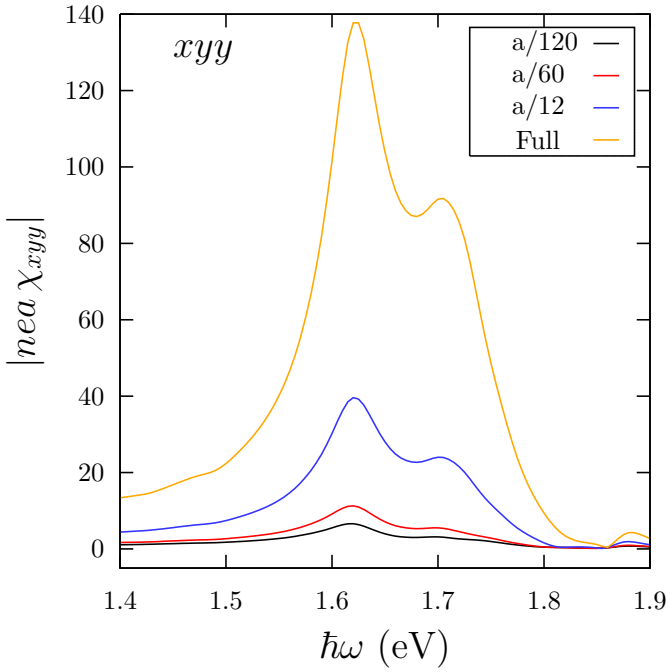

Figure 2.7: Contributions to the quadratic susceptibility χ_{xyy} of the same system as in Fig. 2.6 from the region within a distance Δ from the surface, as defined in Fig. 2.1 for various values of $\Delta = a/120, a/60, a/12$ and compared to the full susceptibility.

3 Comparison with Other Works

In this Chapter, we compare our method of calculation, which includes not only the theoretical approach through the Haydock method but also its numerical implementation, with two methods implemented in other studies. The first one studies rectangular split ring resonators, [91] and the second one hexagonal arrays of nano prisms. [92] The results of the numerical calculations of these systems were compared with theoretical results obtained by Zeng. This comparison readily shows how our method is more flexible and has the great advantage of being implemented in open source software.

3.1 Rectangular Split Ring Resonators

3.1.1 Linear Response

We present results for a metamaterial with a geometry based in a gold nano Split Ring Resonators (SSR) metamaterial. In order to calculate the linear properties of this metamaterial, we used the scheme shown in Chapter 2 to obtain the dielectric function. Then, we proceeded to use that into the characteristic matrix approach, [93] to calculate the reflection, transmission and absortion by a thin film of the metamaterial.

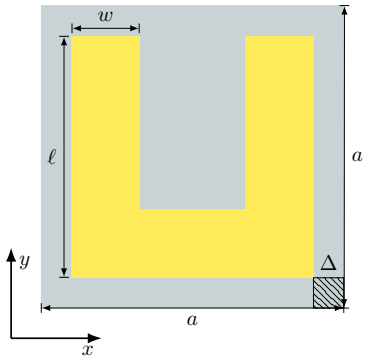

Figure 3.1: Unit cell of a periodic array of SRR. The length ℓ and width w are a fraction of the lattice parameter indicated with a. We indicate the directions x,y of the crystaline axes.

The metamaterial consists of a periodic array of a square unit cell, where gold SSR is placed on a thin film of indium-tin-oxide (ITO) as the host, with a dielectric function $\epsilon = 3.8$, the dielectric function of gold was taken from [94], and the thickness of the SRR and ITO films are 25 and 5nm respectively. These layers are supported by an infinite glass with $\epsilon = 2.25$. Each SRR can be seen as a set of three rectangular gold particles overlapping between them, where the centrosymetry of the system in one principal direction is broken. In order to optimize the geometry, we explored over different configurations of size, length, width and separation of every rectangular particle that compose the unit cell of the array. We matched these results to reach the principal resonance at 1500 nm presented in previous works [37, 91, 95, 96]. For this propose, the parameters of the SRR were $w = \frac{9}{40}a$, $\ell = \frac{4}{5}a$ and $\Delta = \frac{a}{10}$, with ℓ and w the length and the width of a single rectangle of SRR respectively, a the lattice parameter of the square cell and Δ the separation between two contiguous unit cells in the x or y directions and it would be the same at every corner of the square cell. The parameters of the unit cell are shown in Fig. 3.1.

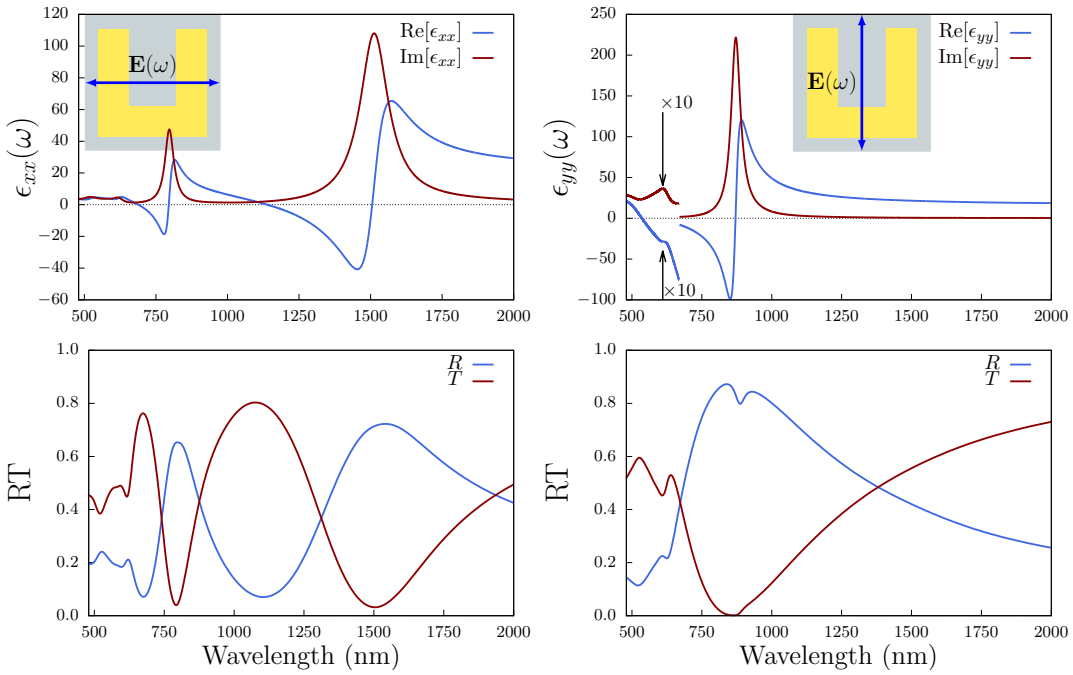

Figure 3.2: Complex dielectric function ϵ_{ii} for a U-shaped Split Ring Resonator (SRR) metamaterial. The yellow region denotes Au and the gray area is the ITO thin film which is dielectric. The blue arrows in the inset of the unit cell indicates the polarization direction of the fundamental electric field $\mathbf{E}(\omega)$. $\epsilon_{yy}(\omega)$ was multiplied by 10 so the resonances below 700 nm could be seen.

In Fig. 3.2, we show in the top row the dielectric function $\epsilon_{xx}(\omega)$ and $\epsilon_{yy}(\omega)$ as a function of the wavelength for two diferent polarizations of the incident electric field, one along $\hat{x}$ and the other along $\hat{y}$, for a infinite 2D array of the SSR sown in Fig. 3.1. When the system is excited with an electric field polarized in the $\hat{x}$ direction, there are two resonances clearly seen in the imaginary part of $\epsilon_{xx}(\omega)$, one around 1521 nm and the other around 797 nm. This could be understood from the fact that along $\hat{x}$ there are to regions where the electric field could resonante, one *inside the U-shape* and the other in the horizontal region of *neighbor unit cells* . Also, for an incident $\hat{y}$ polarized

electric field, there are two resonances in the imaginary part of $\epsilon_{yy}(\omega)$ one around 610 nm ane the other around 870 nm; however, in this case the regions responsible for these resonances of the electric field are between the *vertical regions of neighboring unit cells*, one at the bottom of the U-shape and one at the top of the two arms of the U-shape unit cell.

In the botton row of Fig. 3.2, we show the corresponding transmission (T) and reflectance (R) of the U-shaped SRR metamaterial. The resonances in the dielectric function are seen in the reflection (R) as peaks and in the transmission (T) as deeps, as seen in Fig. 3.2. It is interesting to see how both T and R are related to a fine interference of the real and imaginary parts of the dielectric function, as we could clearly see in the small deeps riding along R and T related to sharp changes of $\epsilon_{yy}(\omega)$.

For a more complete analysis, we confirm that our method based on Haydock's approach comply with Babinet's principle. [97]. Indeed, in Fig. 3.3 we show the complementary structure to that of Fig. 3.2 where the Au and ITO film have been interchanged, and the geometry is kept identical. For this complementary C-SRR metamaterial we have a "complementary" spectrum, where the reflection and transmission have been interchanged; we could take the left (right) column results of Fig. 3.2 and compare them with the right (left) column results of Fig. 3.3 to se that they are almost identical. Indeed, Babinet's principle holds true for ideal perfect conductors, [97] whereas in our case we have a real Au conductor, that nevertheless at infrared wavelengths behaves like an almost ideal conductor. Therefore, knowing the optical behavior of a given metallic metamaterial through Babinet's principle we can extract complementary information about the behavior of the optical response.

Finally, in Fig. 3.4 and 3.5 we show the comparison of our results to those of Ref. [91] where a classical electrodynamic model for the conduction electrons was carried out using a classical Coulomb interacting gas that responds to the electromagnetic field

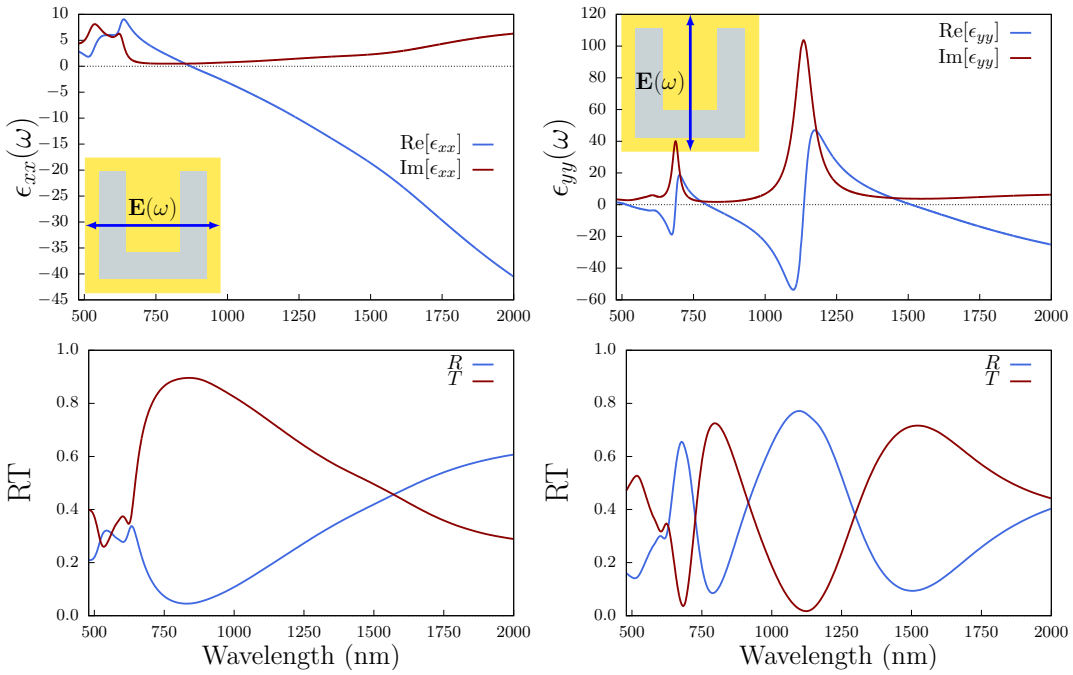

Figure 3.3: Complex dielectric function ϵ_{ii} for a complementary U-shaped Split Ring Resonator (SRR) metamaterial, where the yellow Au region and the gray ITO thin film have been interchanged with those of Fig. 3.2. The blue arrows in the inset of the unit cell indicates the polarization direction of the fundamental electric field $\mathbf{E}(\omega)$.

through the so called plasma equations. Once more, our Haydock's solution to the Maxwell Equations captures the correct physics an reproduces quite accurately the results of Ref. [91]. Moreover, we see that our results have a much better resolution. For example, in the reflection (blue line) of the right-bottom panel an small dip around 880 nm can be observed, that comes from the interplay of the resonances at the corners of the arms of the U-shaped SRR, similar to those shown in Fig. 2.5. To get such dip, we had to use a 600×600 matrix of pixels to described correctly the geometry of the unit cell in order to get converged results. We do not present the analysis since it takes a lengthy explanation along with several figures that go out of the scope of the present

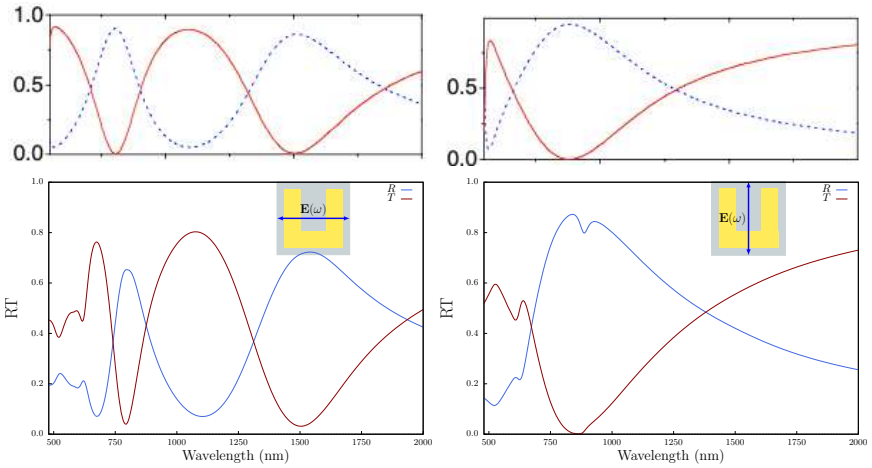

Figure 3.4: T and R comparison of the theoretical results of Ref. [91] (top figures) with our results of Fig. 3.2 (bottom figures). We see very good agreement. The blue arrow in the inset cell of every plot indicates the polarization direction of the fundamental electric field. The x axis scale is the same for all the plots.

Chapter. We could not comment why Ref. [91] does not get such spectroscopic details, as they do not talk about the convergence of their calculation. Our results should be verified by the corresponding experiments.

3.1.2 Second Harmonic Response.

To calculate the SH response, we used the *dipolium* model [79] to retrieve the nonlinear susceptibilities trough the nonlinear polarization. Then, we used the two-layer or Fresnel model to calculate the transmission SH field in optical surfaces. The complete derivation of the SH response is presented in Appendix B.

Our analysis is simplified because we have a system that has a mirror symmetry $x \leftrightarrow -x$ with respect to the center of the unit cell. Thus, the only in-plane non-zero components of the SH susceptibility are [87] χ_{yyy}, χ_{yxx}, and $\chi_{xxy} = \chi_{xyx}$. We omitted

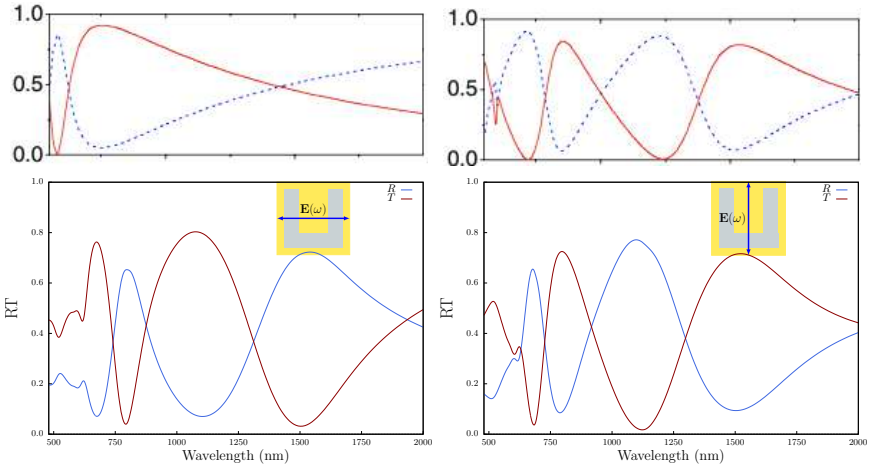

Figure 3.5: Complementary T and R comparison of the theoretical results of Ref. [91] (top figures) with our results of Fig. 3.3 (bottom figures). We see very good agreement. The blue arrow in the inset cell of every plot indicates the polarization direction of the fundamental electric field.

the subindex M and the super-index (2) that indicate these are components of the quadratic macroscopic susceptibility in order to simplify the notation, as this yields no confusion. We calculate the non-zero components for χ_{ijk} in an energy range from 0.6 eV to 1.7 eV for the fundamental field. The absolute value of these components are presented in Fig. 3.6, where two main resonances appear at 0.715 eV and 0.815 eV in the yxx component of χ_{ijk}. The highest resonance located at 0.815 eV matches with the corresponding resonance in the dielectric function for the fundamental fields polarized in the x direction. We expect strong nonlinear response at the double of these frequencies, due to the dipolar character of this resonance, since the structure is non centrosymmetric and the main contribution to the SH polarization is given by the dipolar moment at this energy. Also, several less intense resonances are seen from 1.4 to 1.6 eV, related to the linear resonances of ϵ_{ii} around 1.5 eV as seen in Fig. 3.2.

Once we have the non-zero components of χ_{ijk}, we are able to explore multiples

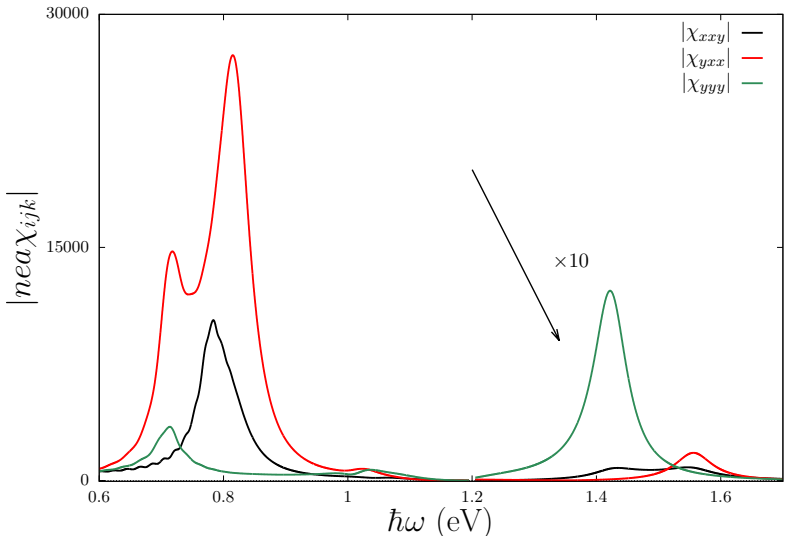

Figure 3.6: Normalized absolute value of $|\chi_{ijk}|$ for a U-shaped SRR with the parameters specified in the text related to Fig. 3.8. We show only the non-zero components of χ_{ijk} due to the symmetry of the system.

aspects of the SH radiation, one of them is the angular dependence of the transmitted SH with respect to the polarization of the fundamental field. For this purpose we consider normal incidence of the incoming fundamental field and the four common polarization combination such as $\mathscr{T}_{pP}$, $\mathscr{T}_{pS}$, $\mathscr{T}_{sP}$, $\mathscr{T}_{sS}$, where the lowercase subindex indicates the incoming polarization of the field and the uppercase subindex indicates the outgoing SH field. The angular dependence in the SHG radiation is observed in Fig. 3.7. As it is shown, the SH field will be polarized in the perpendicular direction with respect to the fundamental field. This result agrees with previous experimental [37, 39, 95] and the theoretical work of Ref. [91], as seen Fig. 3.8. We mention that the rotation of the experimental SHG polar radiation pattern, as explained in [37, 39, 95] may be related to the fact that the geometry of the experimental U-shaped SRR, as shown in Fig. 3.8, has some minor deviations from the theoretical U-shaped SRR. Nevertheless,

the agreement of our calculation based on Haydock's approach is quite good. Needless to say, our method could have used the experimental U-shaped SRR, but this goes beyond the scope of the present work. It should be remarked, tough, that our method yields spectroscopic results that could guide experimentalist to optimize desired experimental applications.

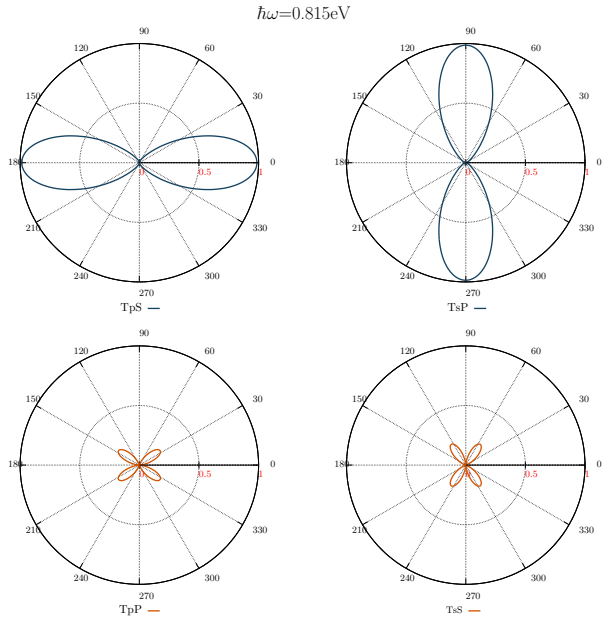

Figure 3.7: Normalized SH transmission field for a SRR with the parameters specified in the text.

3.2 Gold Nano-prisms

In Ref. [92] 2D arrays of metallic Au nano prisms were fabricated using a nano sphere lithography technique described in detailed in Ref. [8]. In summary, a mask of polystyrene nano spheres of 522 nm in diameter are self-assembled in an hexagonal honeycomb structure on the surface of a clean silica glass substrate forming a colloidal layer. Then, Au

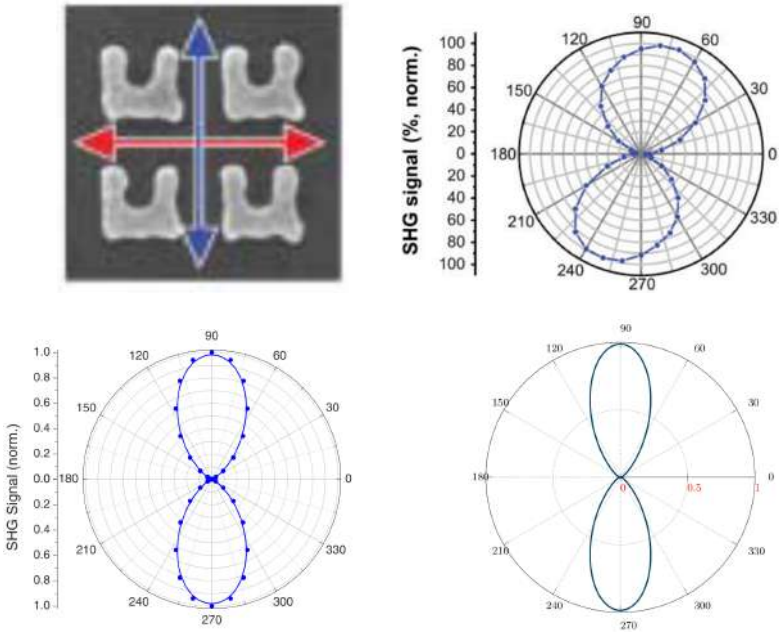

Figure 3.8: Normalized SH transmission intensity for p-in and P-out polarization of the external electric field for a SRR with the parameters specified in the text. The left-top panel shows four representative U-shaped SRR used in the 2D experimental array and the right-top panel shows the normalized SHG radiation patern measured in Ref. [91]. The left bottom panel corresponds to Fig. 2 of the theoretical results given in Ref. [91], and the right bottom panel shows our results. See text for details.

is sprayed by thermal evaporation on the colloidal layer in such a way that the gold only goes to the substate through the intersticial spaces left by the non-overlapping regions of the spheres. In this way, the Au prisms are composed by intersecting circular sections induced by the "circular curvature" of the spheres. Finally the nano spheres are removed by using a solvent, and a silica layer is deposited by magnetron sputtering on the resulting Au nano prisms to prevent possible oxidation effects and physical damage of the nano array. The resulting hexagonal nano structure of gold nano prisms were

observed using a field emission scanning electron microscope as shown at the top of Fig. 3.9.

The measured absorption spectrum of the gold nano prisms sample was taken with unpolarized incident light in Ref. [92] and is shown in Fig. 3.9 with the green line. The spectrum shows a well defined absorption band centered around 1030 nm, which corresponds to the dipolar localized surface plasmon resonance (LSPR) of the nano prisms. The other absorption features at shorter wavelengths correspond to higher order multipolar LSPRs. This assignment of the resonances has been shown by Finite Element Method (FEM) simulations previously performed on similar arrays in Ref. [98].

In Fig. 3.9 we show the micrograph of the experimental system of Ref. [92], along with the theoretical absorbance results as calculated through the Haydock method presented in Chapter 2. In the left middle panel, we show the theoretical unit cell composed by the curvilinear nano prisms, just as those used for the experiment as shown in the top panel. The theoretical absorbance results for these curvilinear gold prisms shown in the right middle panel coincide rather well with the experimental results. Indeed, we see good qualitative agreement in the shape of both the experimental and the theoretical spectra. The dipolar resonance at 1030 nm coincides in wavelength and intensity as do the quadrupolar resonances centered around 700 nm. The overall theoretical absorbance spectrum follows the trend of the experimental absorbance rather well. The differences could be related to imperfections of the experimental array that are unavoidable.

To confirm that on one hand the geometry of the prisms is crucial for the good agreement with the experiment, and on the other hand, that our theoretical Haydock treatment captures such geometry with great detail, in the botom panel of Fig. 3.9 we show the theoretical absorbance for a unit cell of triangular prisms. As can bee seen from the comparison with the experimental results which are for curvilinear prisms, the

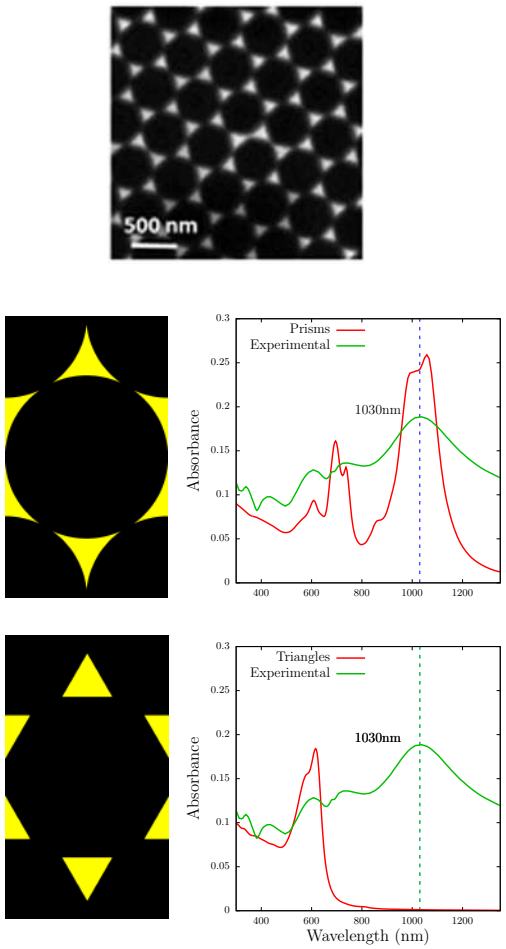

Figure 3.9: We show the experimental micrograph of the system (top panel) used in the absorbance measurements (green line in the middel an bottom panels) presented in Ref. [92]. The red line shows our theoretical absorbance results for the curvilinear (middle panel) and triangular (bottom panel) prisms. See text for details. The unit cells for each calculation are shown in the left column.

disagreement is remarkable. The theoretical result for the triangular prisms only shows the dipolar resonance at 600 nm, in clear disagreement with the experimental results. Our Haydock method is perfectly suited for any shape of both the unit cell and the nano

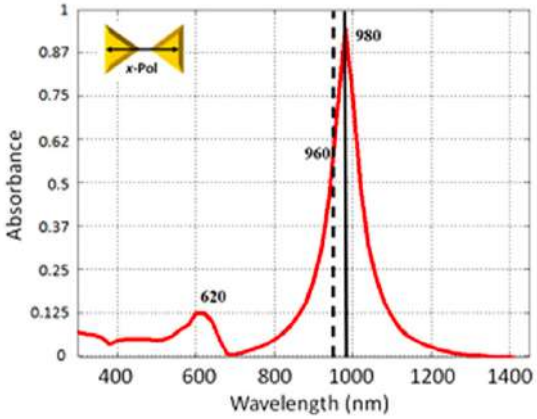

Figure 3.10: We show Fig. 4 of Ref. [92], where the absorbance obtained by the comercial package used by the authors, COMSOL, disagrees with their experimental results shown in Fig. 3.9.

prisms, for which the prisms of Ref. [92] are well reproduced. Therefore, our Haydock approach captures most of the spectral details of the experimental absorbance since we can readily use the correct curvilinear geometry of the prisms.

It is worth mentioning that the simulation done in Ref. [92] considers triangular prisms as the comercial package used by the authors, COMSOL, is incapable of handling curved prisms. Indeed, in Fig. 3.10 we show Fig. 4 of Ref. [92], where the theoretical absorbance calculated with COMSOL is shown. As it can be seen, it disagrees with the experimental results [1] We see how the geometry of the nanoprisms is crucial in order to get agreement with the experiment. Thus, our solution of Maxwell's equations readily captures the physics of such a nice experiment done in Ref. [92].

[1] We mention that the authors claim very good agreement of their numerical results, however as one can see our theoretical scheme reproduces with much more accuracy no only the intensity but also the spectral shape of the experimental results measured by the *same authors.*

4 Conclusions and Final Remarks

4.1 Conclusions

We have developed a formalism for the calculation of the second-order susceptibility of structured binary metamaterials formed by a lattice of particles embedded within a host, for the case where both components consists of centrosymmetric materials, but where the geometry of the inclusion is not centrosymmetric. Although SH is strongly suppressed within a homogeneous centrosymmetric material, the noncentrosymmetric surface is capable of sustaining a surface nonlinear polarization and inducing a strongly varying linear field which produces a multipolar nonlinear polarization within the metamaterial components.

We implemented our formalism using the Haydock recursive scheme within the freely available PHOTONIC modular package and applied it to the calculation of the second order nonlinear susceptibility of a structured metamaterial composed of a homogeneous Ag host with a lattice of pairs of rectangular holes. Although the chosen system is 2D, the formalism may be applied as well to 1D or 3D systems and may be generalized to multicomponent finite systems such as metasurfaces. By modifying the geometry of the

holes, we modify the degree of noncentrosymmetry of the material, allowing us to fine tune both the peak position and intensity of the SH response. The SH signal is very sensitive to changes in the geometrical parameters of the structure.

After establishing the inclusion shape that most enhances this signal, we analyzed the polarization field and showed that the SH response is largest at resonance close to the concave and convex corners but it extends well into the host material. The order of magnitude of the susceptibility obtained in this calculation is comparable to that of typical noncentrosymmetric materials. Although this study was carried out for one particular combination of materials, the employed procedure is equally valid for calculating the nonlinear properties for any metamaterial composed of arbitrary materials and inclusions. Only a priori knowledge of the dielectric function of each constituent material is required. This approach affords the opportunity to quickly and efficiently study a limitless range of possible geometrical configurations in order to optimize the linear and non-linear optical response.

In this sense, we have explored other configurations in the geometry and the composition of the metamaterials, using a nanostructure based on a split-ring resonator and another one based on gold nanoprisms. We show that PHOTONIC is capable of reproducing linear and nonlinear optical experimental results as was shown in Chapter 3. Indeed, we were able to reproduce the experimental results of the split-ring resonators in both the linear and non-linear optical response. Also, we probe that PHOTONIC is better for the calculation of the linear optical response of triangular nano prisms as it can take into account curvilinear shapes, which for instance, COMSOL is incapable of doing. Our solution to Maxwell's equations through the Haydock method is a proficient theoretical and numerical tool for the study of the linear and nonlinear optical properties of nanostructured metamaterials.

4.2 Future work

Further research is required in order to explain some extra details about the origin of the nonlinear optical response in certain metamaterials, specifically in the resonances showed by the nanoresonators. The objective is to expand the Haydock recursive method for the nonlinear response into the retarded regime. This approach could give extra information about the phenomena involved in this response, may capable to extract the magnetic contribution to SH response. Additionally, the proff of Babinet's principle is also needed since this approach could give complementary properties of nanostructured without all the work that it implies. Then, we can analize this principle for the nonlinear response.

As we have mentioned in the introduction of this thesis, we can observe a plethora of nonlinear effects exhibited in metamaterials. Then, it is significant to explore other nonlinear phenomena, using our approach to solve Maxwell's equations in metamaterials. Finally, collaboration with experimental groups would be very relevant for the validation of this thesis. It will also open the possibility to design and fabricate our metamaterials with a specific objective, for example, to use them in nonlinear holography or biosensing.

A Homogenization Procedure and Haydock Recursive Method

In this section, we will explain some relevant details about the *homogenization procedure*, that was developed by Mochán and Barrera. [51,52] In these two articles, they take into account the fluctuations in the electric field due to the inhomogenity of the material in the calculation of macroscopic properties. Then, we will explain the *Haydock Recursion Method*which is used in the calculation of the optical response of a nanostructured metamaterial. This Method was developed by Roger Haydock in 1980 [59], originally as an alternative to the computational solution of the Schrodinger equation. It basically consists on the partial transformation of the Hamiltonian to a tridiagonal matrix works, and what is the analogy between its original porpuse and our approach.

A.1 General Homogenization Procedure

A.1.1 Macroscopic dielectric function

We would like to calculate the effective dielectric response of a periodic composite in the long-wavelength approximation. Simply put, we would like to relate the microscopic

dielectric response $\hat{\boldsymbol{\epsilon}}$, to the macroscopic dielectric response $\hat{\boldsymbol{\epsilon}}^M$, both defined through

$$\mathbf{D} = \hat{\boldsymbol{\epsilon}}\mathbf{E}, \tag{A.1}$$

and

$$\mathbf{D}_a = \hat{\boldsymbol{\epsilon}}^M\mathbf{E}_a, \tag{A.2}$$

where $\mathbf{D}$ ($\mathbf{D}_a$) denote the total (average a) displacement field and $\mathbf{E}$ ($\mathbf{E}_a$) the total (average) electric field. The caret refers to the operator character of both $\hat{\boldsymbol{\epsilon}}$ and $\hat{\boldsymbol{\epsilon}}^M$, which in the space-time representation takes the form

$$\mathbf{D}(\mathbf{r};t) = \int dt' \int d\mathbf{r}'\boldsymbol{\epsilon}(\mathbf{r},\mathbf{r}';t-t')\cdot\mathbf{E}(\mathbf{r}',t'), \tag{A.3}$$

where translational invariance in time has been assumed, and we notice that in general the microscopic dielectric tensor is non-local. A similar expression is satisfied by $\hat{\boldsymbol{\epsilon}}^M$ with $\mathbf{D}$ ($\mathbf{E}$) replaced by $\mathbf{D}_a$ ($\mathbf{E}_a$). We remark that we leave open the possibility for ϵ and ϵ^M to be tensors in Cartesian coordinates, i.e. $\boldsymbol{\epsilon}$ and $\boldsymbol{\epsilon}^M$, respectively. In general, the total fields possess microscopic fluctuations, induced by the microscopic inhomogeneities of the system, which are coupled to the macroscopic fields by the fluctuations of $\hat{\boldsymbol{\epsilon}}$. Since the macroscopic operator $\hat{\boldsymbol{\epsilon}}^M$ relates the average parts of the displacement and electric fields, and averaging procedures is needed to relate $\hat{\boldsymbol{\epsilon}}$ to $\hat{\boldsymbol{\epsilon}}^M$. Such procedure was put forward by Mochán and Barrera, [51] and they showed that in the case of the long wavelength approximation

$$\hat{\boldsymbol{\epsilon}}^M = \hat{\boldsymbol{\epsilon}}_{aa} - \hat{\boldsymbol{\epsilon}}_{af}(\hat{\boldsymbol{\epsilon}}_{ff}^{LL})^{-1}\hat{\boldsymbol{\epsilon}}_{fa}, \tag{A.4}$$

where f denotes the fluctuating part of $\hat{\boldsymbol{\epsilon}}$ and L is related to the longitudinal part of the fields.

The system in question is represented by an arbitrary real space unit cell of volume Ω, with $\mathbf{T}$ representing the lattice translational vectors. We use N unit cells to fill a

volume $V = N\Omega$ and then take the limit of $V \to \infty$ to get the infinite periodic system. Along with the real-space lattice, we introduce the reciprocal lattice expanded by the reciprocal lattice vectors $\mathbf{G}$, that satisfy the standard $\exp(i\mathbf{G}\cdot\mathbf{T}) = 1$ property. Without loss of generality, the time dependence of the fields is chosen to be harmonic, then from Eq. (A.3) we get

$$\mathbf{D}(\mathbf{r};\omega) = \int dt' \int d\mathbf{r}' \boldsymbol{\epsilon}(\mathbf{r},\mathbf{r}';\omega)\cdot\mathbf{E}(\mathbf{r}',\omega), \tag{A.5}$$

where ω is the angular (time) frequency of the fields. From now on, we take the ω dependence of the fields implicit, and only show it explicitly in the dielectric function. The real space invariance requires that

$$\boldsymbol{\epsilon}(\mathbf{r}+\mathbf{T},\mathbf{r}'+\mathbf{T};\omega) = \boldsymbol{\epsilon}(\mathbf{r},\mathbf{r}';\omega), \tag{A.6}$$

and allow us to write

$$\mathbf{E}(\mathbf{r}) = \frac{\Omega}{(2\pi)^3}\int_{BZ} d\mathbf{k} \sum_{\mathbf{G}} E_{\mathbf{k}}(\mathbf{G}) e^{i(\mathbf{k}+\mathbf{G})\cdot\mathbf{r}}, \tag{A.7}$$

and similar equations for the other field of interest, where $\mathbf{k}$ is the Bloch wave vector, whose integral is over the first Brillouin zone. Using Eq. (A.7) and its equivalent for $\mathbf{D}(\mathbf{r})$ in Eq. (A.3) we obtain that

$$\mathbf{D}_{\mathbf{k}}(\mathbf{G}) = \sum_{\mathbf{G}'} \boldsymbol{\epsilon}_{\mathbf{k}}(\mathbf{G},\mathbf{G}';\omega)\mathbf{E}_{\mathbf{k}}(\mathbf{G}'), \tag{A.8}$$

where we find the dielectric matrix (in $\mathbf{G}$ space) as

$$\boldsymbol{\epsilon}_{\mathbf{k}}(\mathbf{G},\mathbf{G}';\omega) = \frac{1}{V}\int_{\omega} d\mathbf{r} \int_{\omega} d\mathbf{r}' \sum_{\mathbf{T}} \boldsymbol{\epsilon}(\mathbf{r}+\mathbf{T},\mathbf{r}';\omega) e^{-i[(\mathbf{k}+\mathbf{G})\cdot(\mathbf{r}+\mathbf{T})-(\mathbf{k}+\mathbf{G}')\cdot\mathbf{r}']}. \tag{A.9}$$

To proceed further, we assume that the microscopic dielectric function is local, i.e.

$$\boldsymbol{\epsilon}(\mathbf{r},\mathbf{r}';\omega) = \boldsymbol{\epsilon}(\mathbf{r};\omega)\delta(\mathbf{r}-\mathbf{r}'), \tag{A.10}$$

still with $\boldsymbol{\epsilon}(\mathbf{r};\omega) = \boldsymbol{\epsilon}(\mathbf{r}+\mathbf{T};\omega)$. Using Eq. (A.10) in Eq. (A.9), we obtain

$$\boldsymbol{\epsilon}_{\mathbf{k}}(\mathbf{G},\mathbf{G}';\omega) = \frac{1}{\Omega}\int_{\Omega} d\mathbf{r}\boldsymbol{\epsilon}(\mathbf{r};\omega) e^{-i(\mathbf{G}-\mathbf{G}')\cdot\mathbf{r}}, \tag{A.11}$$

where we used $\sum_{\mathbf{T}} \exp(i\mathbf{G}\cdot\mathbf{T}) = N$, and we notice that the there is no dependence on $\mathbf{k}$ in view of the locality of $\boldsymbol{\epsilon}$, and thus we drop it from the sub-index.

Following Mochán and Barrera, [52] we chose as an averaging procedure a truncation that eliminates all the wave vectors outside the first Brillouin zone, then the average for any function $\mathcal{F}_{\mathbf{k}}(\mathbf{G})$ is simply given by

$$(\mathcal{F}_a)_{\mathbf{k}}(\mathbf{G}) \equiv \mathcal{F}_{\mathbf{k}}(\mathbf{G}=0)\delta_{\mathbf{G},0}. \tag{A.12}$$

Therefore, in very simple words, the $\mathbf{G}=0$ term give the (a) average values, whereas the $\mathbf{G}\neq 0$ terms give the (f) fluctuating values, with which we easily write Eq. (A.4) as

$$\boldsymbol{\epsilon}^{M}(\omega) = \boldsymbol{\epsilon}(\mathbf{G}=0,\mathbf{G}'=0;\omega) - \sum_{\mathbf{G},\mathbf{G}'(\neq 0)} \boldsymbol{\epsilon}(\mathbf{G}=0,\mathbf{G};\omega)[\boldsymbol{\epsilon}^{LL}(\mathbf{G},\mathbf{G}';\omega;\mathbf{k})]^{-1}\boldsymbol{\epsilon}(\mathbf{G}',\mathbf{G}=0;\omega). \tag{A.13}$$

Now, in this reciprocal lattice representation, we introduce, $\mathbf{P}^{L}_{\mathbf{k}}(\mathbf{G})$,

$$\mathbf{P}^{L}_{\mathbf{k}}(\mathbf{G}) = \frac{\mathbf{k}+\mathbf{G}}{|\mathbf{k}+\mathbf{G}|}\frac{\mathbf{k}+\mathbf{G}}{|\mathbf{k}+\mathbf{G}|}, \tag{A.14}$$

as a longitudinal projector, such that

$$\boldsymbol{\epsilon}^{LL}(\mathbf{G},\mathbf{G}';\omega;\mathbf{k}) = \mathbf{P}^{L}_{\mathbf{k}}(\mathbf{G})\cdot\boldsymbol{\epsilon}(\mathbf{G},\mathbf{G}';\omega)\cdot\mathbf{P}^{L}_{\mathbf{k}}(\mathbf{G}'), \tag{A.15}$$

is the longitudinal-longitudinal component of $\boldsymbol{\epsilon}(\mathbf{G},\mathbf{G}';\omega)$. Then, applying $\mathbf{P}^{L}_{\mathbf{k}}(\mathbf{G})$ to Eq. (A.13), and putting the $\mathbf{G}$ as sub-indices, we get

$$\boldsymbol{\epsilon}^{M,LL}(\omega) = \boldsymbol{\epsilon}^{LL}_{00}(\omega) - \sum_{\mathbf{G},\mathbf{G}'(\neq 0)} \boldsymbol{\epsilon}^{LL}_{0\mathbf{G}}(\omega)[\boldsymbol{\epsilon}^{LL}_{\mathbf{G}\mathbf{G}'}(\omega;\mathbf{k})]^{-1}\boldsymbol{\epsilon}^{LL}_{\mathbf{G}'0}(\omega), \tag{A.16}$$

where from Eq. (A.11)

$$\boldsymbol{\epsilon}_{\mathbf{G}\mathbf{G}'}(\omega) = \frac{1}{\Omega}\int_{\Omega} d\mathbf{r}\boldsymbol{\epsilon}(\mathbf{r};\omega)e^{-i(\mathbf{G}-\mathbf{G}')\cdot\mathbf{r}}. \tag{A.17}$$

According to Eq. (A.4), the matrix to be inverted is that of the fluctuating-fluctuating contributions, and we see that form Eq. (A.16), that $\boldsymbol{\epsilon}^{LL}_{\mathbf{G}\mathbf{G}'}(\omega;\mathbf{k})$ should be constructed only for all the values for which $\mathbf{G}$ and $\mathbf{G}'$ are different from zero, i.e. only the fluctuating terms, and then, it should be inverted.

In general, Eq. (A.16) could be solved as follows. We write, in $\mathbf{G}$ space,

$$\boldsymbol{\epsilon}^{LL}_{\mathbf{G}\mathbf{G}'} = \begin{pmatrix} \boldsymbol{\epsilon}^{LL}_{00} & \boldsymbol{\epsilon}^{LL}_{0\mathbf{G}'} \\ \boldsymbol{\epsilon}^{LL}_{\mathbf{G}0} & \boldsymbol{\epsilon}^{LL}_{\mathbf{G}\mathbf{G}'} \end{pmatrix}, \tag{A.18}$$

and its inverse as

$$(\boldsymbol{\epsilon}^{LL}_{\mathbf{G}\mathbf{G}'})^{-1} = \begin{pmatrix} \mathbf{a} & \mathbf{b} \\ \mathbf{c} & \mathbf{d} \end{pmatrix}, \tag{A.19}$$

where it should be clear that for all the sub-indices not explicitly written as zero, $\mathbf{G}, \mathbf{G}' \neq 0$. In particular $\mathbf{a} = [\boldsymbol{\epsilon}^{LL}_{\mathbf{G}\mathbf{G}'}]^{-1}|_{00}$. Since, $\sum_{\mathbf{G}''}(\boldsymbol{\epsilon}^{LL}_{\mathbf{G}\mathbf{G}''})^{-1}\boldsymbol{\epsilon}^{LL}_{\mathbf{G}''\mathbf{G}'} = \delta_{\mathbf{G}\mathbf{G}'}$, we can formally solve for $\mathbf{a}$, $\mathbf{b}$, $\mathbf{c}$, and $\mathbf{d}$. For instance, we get that

$$\boldsymbol{\epsilon}^{LL}_{00}\mathbf{a} + \boldsymbol{\epsilon}^{LL}_{0\mathbf{G}'}\mathbf{c} = 1, \tag{A.20a}$$

$$\boldsymbol{\epsilon}^{LL}_{\mathbf{G}0}\mathbf{a} + \boldsymbol{\epsilon}^{LL}_{\mathbf{G}\mathbf{G}'}\mathbf{c} = 0. \tag{A.20b}$$

From Eq. (A.20b), we solve for $\mathbf{c}$, and substitute into Eq. (A.20a) to find

$$\mathbf{a}^{-1} = \boldsymbol{\epsilon}^{LL}_{00} - \sum_{\mathbf{G},\mathbf{G}'\neq 0} \boldsymbol{\epsilon}^{LL}_{0\mathbf{G}}\boldsymbol{\epsilon}^{LL}_{\mathbf{G}\mathbf{G}'}\boldsymbol{\epsilon}^{LL}_{\mathbf{G}'0}. \tag{A.21}$$

Now, comparing with the right hand side of Eq. (A.16), we see that $\boldsymbol{\epsilon}^{M,LL} = \mathbf{a}^{-1}$, or

$$[\boldsymbol{\epsilon}^{M,LL}]^{-1} = \left(\boldsymbol{\epsilon}^{LL}_{\mathbf{G}\mathbf{G}'}\right)^{-1}\Big|_{00}, \tag{A.22}$$

where one has to construct $\boldsymbol{\epsilon}^{LL}_{\mathbf{G}\mathbf{G}'}$ for all values of $\mathbf{G}, \mathbf{G}'$, invert and then take the $\mathbf{G} = \mathbf{G}' = 0$ component. As discussed by Mochán and Barrera, [52] this results was first obtained by Alder [99] and Wiser [100].

From Eq. (A.22) and Eq. (A.17) we see that all we need to compute the macroscopic dielectric function, $\boldsymbol{\epsilon}^M$ (Eq. (A.22)), within the long wave length approximation, is the knowledge of $\boldsymbol{\epsilon}(\mathbf{r};\omega)$ and the specification of the real-space unit cell (that it turns determines the reciprocal lattice vectors $\mathbf{G}$).

A.1.2 Two-component system

We consider, without loss of generality, a two-component system with an arbitrary unit cell, where the host (the interstitial region) is characterized with $\boldsymbol{\epsilon}_b(\omega)$, and the inclusion, with volume v and arbitrary shape, is characterized with $\boldsymbol{\epsilon}_a(\omega)$. (see Fig. A.1). Then, from Eq. (A.17)

$$\begin{aligned}\boldsymbol{\epsilon}_{\mathbf{GG'}}(\omega) &= \frac{\boldsymbol{\epsilon}_a(\omega)-\boldsymbol{\epsilon}_b(\omega)}{\Omega}\int_v d\mathbf{r}e^{i\mathbf{r}\cdot(\mathbf{G}-\mathbf{G'})}+\frac{\boldsymbol{\epsilon}_b(\omega)}{\Omega}\int_\Omega d\mathbf{r}e^{i\mathbf{r}\cdot(\mathbf{G}-\mathbf{G'})}\\ &= \boldsymbol{\epsilon}_{ab}(\omega)\mathbf{F}_{\mathbf{GG'}}+\boldsymbol{\epsilon}_b(\omega)\delta_{\mathbf{GG'}},\end{aligned} \tag{A.23}$$

where $\boldsymbol{\epsilon}_{ab}(\omega)=\boldsymbol{\epsilon}_a(\omega)-\boldsymbol{\epsilon}_b(\omega)$, and

$$\mathbf{F}_{\mathbf{GG'}}=\frac{1}{\Omega}\int_v e^{i\mathbf{r}\cdot(\mathbf{G}-\mathbf{G'})}d\mathbf{r}, \tag{A.24}$$

as the Fourier coefficient of the inclusion. Indeed, we can write

$$\mathbf{F}_{\mathbf{GG'}}=\frac{1}{\Omega}\int_\Omega F(\mathbf{r})e^{i\mathbf{r}\cdot(\mathbf{G}-\mathbf{G'})}d\mathbf{r}, \tag{A.25}$$

where

$$F(\mathbf{r})=\begin{cases}1 & \text{if } \mathbf{r}\in \text{inclusion}\\ 0 & \text{other wise}\end{cases}, \tag{A.26}$$

Note that in particular

$$F_{00}=\frac{1}{\Omega}\int_v d\mathbf{r}=\frac{v}{\Omega}\equiv f. \tag{A.27}$$

with $f=v/\Omega$ the filling fraction of the inclusions. We notice that in real-space $F(\mathbf{r})$ is a scalar function, whereas in reciprocal space $\mathbf{F}_{\mathbf{GG'}}$ is a matrix.

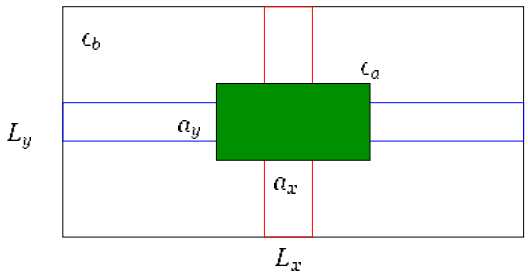

Figure A.1: (color online) We show the 2D unit cell of the system. The inclusion (interstitial) is represented by ϵ_a (ϵ_b). The elongated rectangles represent the two extreme cases for the inclusion as we deform it keeping the filling fraction fixed (see text for details).

Projecting the longitudinal part of Eq. (A.23), (applying Eq. (A.14)) we obtain,

$$\boldsymbol{\epsilon}^{LL}_{\mathbf{GG'}}(\omega) = \hat{\mathbf{G}}\hat{\mathbf{G}} \cdot \boldsymbol{\epsilon}_{\mathbf{GG'}}(\omega) \cdot \hat{\mathbf{G}}'\hat{\mathbf{G}}' = \hat{\mathbf{G}}\boldsymbol{\epsilon}^{LL}_{\mathbf{GG'}}(\omega)\hat{\mathbf{G}}', \tag{A.28}$$

with $\hat{\mathbf{G}} = \mathbf{G}/|\mathbf{G}|$. Here, $\boldsymbol{\epsilon}^{LL}_{\mathbf{GG'}}(\omega)$ is given by

$$\boldsymbol{\epsilon}^{LL}_{\mathbf{GG'}}(\omega) = \boldsymbol{\epsilon}_b(\omega)\delta_{\mathbf{GG'}} + \boldsymbol{\epsilon}_{ab}(\omega)\mathbf{F}^{LL}_{\mathbf{GG'}}, \tag{A.29}$$

with

$$\mathbf{F}^{LL}_{\mathbf{GG'}} = \hat{\mathbf{G}}\mathbf{F}_{\mathbf{GG'}}\hat{\mathbf{G}}'. \tag{A.30}$$

Now, the inverse

$$[\boldsymbol{\epsilon}^{LL}_{\mathbf{GG'}}(\omega)]^{-1} = \hat{\mathbf{G}}[\hat{\mathbf{G}} \cdot \boldsymbol{\epsilon}_{\mathbf{GG'}}(\omega) \cdot \hat{\mathbf{G}}']^{-1}\hat{\mathbf{G}}' = \hat{\mathbf{G}}[\boldsymbol{\epsilon}^{LL}_{\mathbf{GG'}}(\omega)]^{-1}\hat{\mathbf{G}}', \tag{A.31}$$

gives the expected result $\sum_{\mathbf{G''}} \boldsymbol{\epsilon}^{LL}_{\mathbf{GG''}}(\omega)[\boldsymbol{\epsilon}^{LL}_{\mathbf{G''G'}}(\omega)]^{-1} = \hat{\mathbf{G}}\hat{\mathbf{G}}\delta_{\mathbf{GG'}}$. From Eq. (A.29) we write

$$[\boldsymbol{\epsilon}^{LL}_{\mathbf{GG'}}(\omega)]^{-1} = [\boldsymbol{\epsilon}_{ab}\left((\boldsymbol{\epsilon}_{ab})^{-1}\boldsymbol{\epsilon}_b(\omega)\delta_{\mathbf{GG'}} + \mathbf{F}^{LL}_{\mathbf{GG'}}\right)]^{-1}, \tag{A.32}$$

that for optically isotropic host and inclusion, reduces to

$$[\boldsymbol{\epsilon}^{LL}_{\mathbf{GG'}}(\omega)]^{-1} = \frac{1}{\epsilon_{ab}(\omega)}[u(\omega)\delta_{\mathbf{GG'}} + \mathbf{F}^{LL}_{\mathbf{GG'}}]^{-1}, \tag{A.33}$$

where $u(\omega) = \epsilon_b(\omega)/\epsilon_{ab}(\omega)$.

$$\frac{1}{\epsilon_M^{LL}} = \frac{u(\omega)}{\epsilon_b(\omega)} \left[u(\omega)\delta_{\mathbf{GG'}} + \mathbf{F}_{\mathbf{GG'}}^{LL}\right]^{-1}\Big|_{00}, \tag{A.34}$$

A.1.3 Haydock's method Fundamentals

Suppose we have a Hamiltonian H for which one would like to calculate a given expectation value of the Green function, i.e.

$$\langle 0|(E-H)^{-1}|0\rangle, \tag{A.35}$$

where E are the associated eigenvalues. The Haydock's method basically consist of changing to a new basis (in the Hilbert space) in which the Hamiltonian is a tridiagonal matrix. Thus we start from the ket of interest, i.e. $|0\rangle$, and construct a new ket as follows:

$$|\tilde{1}\rangle = H|0\rangle, \tag{A.36}$$

where we write

$$|\tilde{1}\rangle = a_0|0\rangle + b_1|1\rangle, \tag{A.37}$$

as a linear combination of "regular" kets $|0\rangle$ and $|1\rangle$. These regular kets are orthonormalized, $\langle i|j\rangle = \delta_{ij}$. Then

$$a_0 = \langle 0|H|0\rangle, \tag{A.38}$$

and from the norm

$$\langle\tilde{1}|\tilde{1}\rangle = a_0^2 + b_1^2 = \||H|0\rangle\|^2, \tag{A.39}$$

we obtain b_1, and from Eq. (A.37) we obtain

$$|1\rangle = \frac{|\tilde{1}\rangle - a_0|0\rangle}{b_1}, \tag{A.40}$$

that is properly normalized. Recall that $\|H|0\rangle\|^2 = \langle 0|H^\dagger H|0\rangle$ and that $H = H^\dagger$ (hermitian operator).

Now, we construct our second ket,

$$|\tilde{2}\rangle = H|1\rangle, \tag{A.41}$$

and

$$|\tilde{2}\rangle = b_1|0\rangle + a_1|1\rangle + b_2|2\rangle, \tag{A.42}$$

where

$$a_1 = \langle 1|\tilde{2}\rangle = \langle 1|H|1\rangle, \tag{A.43}$$

$$b_1 = \langle 0|\tilde{2}\rangle = \langle 0|H|1\rangle, \tag{A.44}$$

and from the norm

$$\langle \tilde{2}|\tilde{2}\rangle = a_0^2 + b_1^2 + b_2^2, \tag{A.45}$$

we solve for b_2, and then from Eq. (A.42)

$$|2\rangle = \frac{|\tilde{2}\rangle - b_1|0\rangle - a_1|1\rangle}{b_2}. \tag{A.46}$$

We finally move the third ket

$$|\tilde{3}\rangle = H|2\rangle, \tag{A.47}$$

but before writing it as a linear combination of regular kets, we notice that

$$\langle 0|\tilde{3}\rangle = \langle 0|H|2\rangle = \langle \tilde{1}|2\rangle = (a_0\langle 0| + b_1\langle 1|)|2\rangle = 0, \tag{A.48}$$

where we used the transpose of Eq. (A.36) and Eq. (A.37), so the new kets only couple nearest neighbors kets. Then,

$$|\tilde{3}\rangle = b_2|1\rangle + a_2|2\rangle + b_3|3\rangle, \tag{A.49}$$

where

$$a_2 = \langle 2|\tilde{3}\rangle = \langle 2|H|2\rangle, \tag{A.50}$$

$$b_2 = \langle 1|\tilde{3}\rangle = \langle 1|H|2\rangle, \tag{A.51}$$

and from the norm

$$\langle \tilde{3}|\tilde{3}\rangle = b_2^2 + a_2^2 + b_3^2, \tag{A.52}$$

we solve for b_3, and then from Eq. (A.49)

$$|3\rangle = \frac{|\tilde{3}\rangle - b_2|1\rangle - a_2|2\rangle}{b_3}. \tag{A.53}$$

From this point on, the method just keeps repeating, so we can write that in general, that

$$|\widetilde{n+1}\rangle = H|n\rangle, \tag{A.54}$$

$$a_n = \langle n|\widetilde{n+1}\rangle = \langle n|H|n\rangle, \tag{A.55}$$

$$b_n = \langle n-1|\widetilde{n+1}\rangle = \langle n-1|H|n\rangle, \tag{A.56}$$

and

$$\langle n-m|\widetilde{n+1}\rangle = 0 \quad \forall m2, \tag{A.57}$$

with which

$$|\widetilde{n+1}\rangle = b_n|n-1\rangle + a_n|n\rangle + b_{n+1}|n+1\rangle. \tag{A.58}$$

From,

$$\left\||\widetilde{n+1}\rangle\right\|^2 = b_n^2 + a_n^2 + b_{n+1}^2, \tag{A.59}$$

we find the b_{n+1} term. Indeed, we do not need to use Eq. (A.56) for the b_n terms, instead we use Eq. (A.59) to find first $b_1 = \||\tilde{1}\rangle\|^2 - a_0^2$, since by construction $b_0 = 0$, where $|\tilde{1}\rangle = H|0\rangle$, and we chose what $|0\rangle$ should be. Then, we can iterate Eq. (A.59) once more for b_2, once we have calculated a_2 form Eq. (A.55), and we proceed likewise for all the $b_{n>2}$. From Eq. (A.58) we finally obtain

$$|n+1\rangle = \frac{|\widetilde{n+1}\rangle - b_n|n-1\rangle - a_n|n\rangle}{b_{n+1}}, \tag{A.60}$$

where by construction $|-1\rangle = 0$. Using the $|n\rangle$ basis we can write the Hamiltonian as

$$H = \begin{pmatrix} a_0 & b_1 & 0 & 0 & 0 & \cdots \\ b_1 & a_1 & b_2 & 0 & 0 & \cdots \\ 0 & b_2 & a_2 & b_3 & 0 & \cdots \\ 0 & 0 & b_3 & a_3 & b_4 & \cdots \\ \vdots & \vdots & & \ddots & \ddots & \ddots \end{pmatrix}, \tag{A.61}$$

which is a tridiagonal matrix.

Now, let us take the function, $G = E - H$, which is written as

$$G_0 = \left(\begin{array}{c|cccc} E - a_0 & -b_1 & 0 & 0 & 0 & \cdots \\ \hline -b_1 & E - a_1 & -b_2 & 0 & 0 & \cdots \\ 0 & -b_2 & E - a_2 & -b_3 & 0 & \cdots \\ 0 & 0 & -b_3 & E - a_3 & -b_4 & \cdots \\ \vdots & \vdots & & \ddots & \ddots & \ddots \end{array}\right), \tag{A.62}$$

and rewritten as

$$G_0 = \left(\begin{array}{c|c} A_0 & B_1 \\ \hline B_1^T & G_1 \end{array}\right), \tag{A.63}$$

where $A_0 = E - a_0$, $B_1 = (-b_1, 0, 0, \cdots)$ and

$$G_1 = \left(\begin{array}{c|cccc} E - a_1 & -b_2 & 0 & 0 & \cdots \\ \hline -b_2 & E - a_2 & -b_3 & 0 & \cdots \\ 0 & -b_3 & E - a_3 & -b_4 & \cdots \\ \vdots & \vdots & \ddots & \ddots & \ddots \end{array}\right). \tag{A.64}$$

So we see that we can generalize this block representation to

$$G_n = \left(\begin{array}{c|c} A_n & B_{n+1} \\ \hline B_{n+1}^T & G_{n+1} \end{array}\right), \tag{A.65}$$

where $A_n = E - a_n$, $B_n = (-b_n, 0, 0, \cdots)$ and

$$G_n = \left(\begin{array}{c|cccc} E-a_n & -b_{n+1} & 0 & 0 & \cdots \\ \hline -b_{n+1} & E-a_{n+1} & -b_{n+2} & 0 & \cdots \\ 0 & -b_{n+2} & E-a_{n+2} & -b_{n+3} & \cdots \\ \vdots & \vdots & \ddots & \ddots & \ddots \end{array}\right). \tag{A.66}$$

We can invert any given G_n as follows. Call M_n its inverse, and write

$$M_n = \left(\begin{array}{c|c} R_n & P_n \\ \hline Q_n & S_n \end{array}\right), \tag{A.67}$$

where it follows, that in particular,

$$A_n R_n + B_{n+1} Q_n = 1, \tag{A.68a}$$

$$B_{n+1}^T R_n + G_{n+1} Q_n = 0, \tag{A.68b}$$

Eq. (A.68b) gives $Q_n = -G_{n+1}^{-1} B_{n+1}^T R$, that when substituted in Eq. (A.68a) leads to

$$\begin{aligned} R_n &= (A_n - B_{n+1} G_{n+1}^{-1} B_{n+1}^T)^{-1} \\ &= \frac{1}{A_n - B_{n+1} G_{n+1}^{-1} B_{n+1}^T}, \end{aligned} \tag{A.69}$$

where we see that the n-order solution is linked to the $n+1$-order solution, since G_{n+1}^{-1} is unknown, but the same recursive solution, would give its value, in terms of the next term, where G_{n+2}^{-1} is again unknown, and so forth. Note that A_n is a simple scalar function and after proper multiplication, $B_{n+1} G_{n+1}^{-1} B_{n+1}^T$ is also scalar.

Going back to our original problem, we see that

$$\langle 0|(E-H)^{-1}|0\rangle \equiv [(E-H)^{-1}]_{00} = R_0, \tag{A.70}$$

but since R_0 is related R_1 and this to R_2 and so forth, is easy to see that the final results is given by

$$\langle 0|(E-H)^{-1}|0\rangle = \cfrac{1}{E - a_0 - \cfrac{b_1^2}{E-a_1-\cfrac{b_2^2}{E-a_2-\cfrac{b_3^2}{\vdots}}}}, \tag{A.71}$$

which is a continued fraction (Haydock) expansion "ad-infinitum". In practice, the continued fraction converges to a fixed value after n-terms. In summary the method consist of evaluating the Haydock coefficients of Eq. (A.55) and Eq. (A.56), following the prescription explained above, and use these a_n and b_n coefficients in above expansion. If one would like to proceed with direct inversion of the Green's function, the problem could be numerically very costly, whereas evaluating hundreds of Haydock coefficients, typically enough to converge the continued fraction, is numerically very cheap.

A.1.4 Implementation of the Haydock method

In this subsection we show how to implement Haydock's method for the calculation of Eq. (A.34). Indeed, the mapping of our problem to the Haydock's method is rather straightforward, once we identify

$$|0\rangle \leftarrow \delta_{\mathbf{G}0} \quad u \leftarrow E \quad \mathbf{F}^{LL}_{\mathbf{G}\mathbf{G}'} \leftarrow H, \tag{A.72}$$

and the Hilbert space with the reciprocal-lattice ($\mathbf{G}$) space, where the kets are orthonormalized, i.e. $\langle \mathbf{G}|\mathbf{G}'\rangle = \delta_{\mathbf{G}\mathbf{G}'}$. Thus we get,

$$\frac{1}{\epsilon^{M,LL}} = \frac{u(\omega)}{\epsilon_b(\omega)} \cfrac{1}{u(\omega) - a_0 - \cfrac{b_1^2}{u(\omega)-a_1-\cfrac{b_2^2}{u(\omega)-a_2-\cfrac{b_3^2}{\vdots}}}}, \tag{A.73}$$

so all we have to do is generate the Haydock coefficients a_n and b_n. We remark that with this method, one separates the geometry of the unit cell and the inclusion from the optical properties of the host and the inclusion. Indeed, the Haydock coefficients a_n and b_n solely depend on such geometry, whereas the optical response of the constituent materials only enters above expression through $\epsilon_a(\omega)$ and $\epsilon_b(\omega)$ ($u(\omega) = \epsilon_b(\omega)/\epsilon_{ab}(\omega)$). Thus, for a given geometry one can trivially explore a whole set of very different materials.

We start with the calculation of $a_n = \langle n|\widetilde{n+1}\rangle$. So we take,

$$\begin{aligned} |\widetilde{n+1}\rangle = H|n\rangle &= \sum_{\mathbf{G}\mathbf{G}'} |\mathbf{G}\rangle\langle\mathbf{G}|H|\mathbf{G}'\rangle\langle\mathbf{G}'|n\rangle \\ &= \sum_{\mathbf{G}\mathbf{G}'} |\mathbf{G}\rangle \mathbf{F}^{LL}_{\mathbf{G}\mathbf{G}'}\varphi_n(\mathbf{G}') \\ &= \sum_{\mathbf{G}\mathbf{G}'} |\mathbf{G}\rangle \hat{\mathbf{G}}\cdot\mathbf{F}_{\mathbf{G}\mathbf{G}'}\cdot\hat{\mathbf{G}}'\varphi_n(\mathbf{G}') \\ &= \sum_{\mathbf{G}\mathbf{G}'} |\mathbf{G}\rangle \hat{\mathbf{G}}\cdot\mathbf{F}_{\mathbf{G}\mathbf{G}'}\vec{\varphi}_n(\mathbf{G}') \\ &= \sum_{\mathbf{G}} |\mathbf{G}\rangle \hat{\mathbf{G}}\cdot\vec{\psi}_n(\mathbf{G}), \end{aligned} \tag{A.74}$$

using the closure relation $\sum_{\mathbf{G}} |\mathbf{G}\rangle\langle\mathbf{G}| = 1$, Eq. (A.30), and defining,

$$\varphi_n(\mathbf{G}) = \langle\mathbf{G}|n\rangle, \tag{A.75}$$

$$\vec{\varphi}_n(\mathbf{G}) = \hat{\mathbf{G}}\varphi_n(\mathbf{G}), \tag{A.76}$$

and

$$\vec{\psi}_n(\mathbf{G}) = \sum_{\mathbf{G}'} \mathbf{F}_{\mathbf{G}\mathbf{G}'}\vec{\varphi}_n(\mathbf{G}'), \tag{A.77}$$

where the arrow denotes a vector in $\mathbf{G}$-space. Now,

$$\langle\mathbf{G}|H|n\rangle = \langle\mathbf{G}|\widetilde{n+1}\rangle = \varphi_{\widetilde{n+1}}(\mathbf{G}) = \hat{\mathbf{G}}\cdot\vec{\psi}_n(\mathbf{G}), \tag{A.78}$$

where the second equality comes from the definition of Eq. (A.75), and the last equality comes from Eq. (A.74). Therefore,

$$\begin{aligned} a_n = \langle n|\widetilde{n+1}\rangle &= \sum_{\mathbf{G}} \langle n|\mathbf{G}\rangle\langle \mathbf{G}|H|n\rangle \\ &= \sum_{\mathbf{G}} \varphi_n^{\dagger}(\mathbf{G})\varphi_{\widetilde{n+1}}(\mathbf{G}), \end{aligned} \tag{A.79}$$

with which we obtain b_{n+1} through Eq. (A.59), and from Eq. (A.58)

$$\varphi_{n+1}(\mathbf{G}) = \frac{\varphi_{\widetilde{n+1}}(\mathbf{G}) - a_n\varphi_n(\mathbf{G}) - b_n\varphi_{n-1}(\mathbf{G})}{b_{n+1}}, \tag{A.80}$$

that should be used iteratively starting from $n = 0$, once we have chosen the initial state $\varphi_0(\mathbf{G})$. Since we are interested in the $\mathbf{G} = 0$-$\mathbf{G} = 0$ component, we chose $\varphi_0(\mathbf{G}) = \langle \mathbf{G}|0\rangle = \delta_{\mathbf{G}0}$.

A.1.4.1 Numerical Shortcut

We interpret $\vec{\varphi}_n(\mathbf{G})$ and $\vec{\psi}_n(\mathbf{G})$ as the Fourier coefficients of a real-space functions $\vec{\varphi}_n(\mathbf{r})$ and $\vec{\psi}_n(\mathbf{r})$, respectively, such that

$$\vec{\varphi}_n(\mathbf{G}) = \int d\mathbf{r}\vec{\varphi}_n(\mathbf{r})e^{i\mathbf{G}\cdot\mathbf{r}}, \tag{A.81}$$

and

$$\vec{\psi}_n(\mathbf{G}) = \int d\mathbf{r}\vec{\psi}_n(\mathbf{r})e^{i\mathbf{G}\cdot\mathbf{r}}. \tag{A.82}$$

But now, from Eq. (A.25) we see that $\mathbf{F}_{\mathbf{G}\mathbf{G}'} = \mathbf{F}(\mathbf{G} - \mathbf{G}')$, and thus Eq. (A.77) is the convolution of $\vec{\psi}_n(\mathbf{r}) = \vec{\varphi}_n(\mathbf{r})F(\mathbf{r})$, where $F(\mathbf{r})$ is given in Eq. (A.26). This result is of great numerical importance, since instead of calculating the usually complicated $\mathbf{F}(\mathbf{G} - \mathbf{G}')$ and doing the sum over $\mathbf{G}'$, as required by Eq. (A.77) for every $\mathbf{G}$, we can multiply in real-space $F(\mathbf{r})$ and $\vec{\varphi}_n(\mathbf{r})$, and the transform back to Fourier space ($\mathbf{G}$) to obtain $\vec{\psi}_n(\mathbf{G})$. Thus, we can basically define any shape of the inclusion in real-space without even knowing how its Fourier transform looks like!

Once we have $\vec{\psi}_n(\mathbf{G})$ we dot product it with $\hat{\mathbf{G}}$ to get $\widetilde{\varphi_{n+1}}(\mathbf{G})$. Now, $\varphi_n(\mathbf{G})$ is generated according to Eq. (A.60), starting from the initial sate $\langle \mathbf{G}|0\rangle = \delta_{\mathbf{G}0}$. The state $\varphi_n(\mathbf{G})$ is Fourier transformed to get $\varphi_n(\mathbf{r})$. Then, above procedure give us a complete set of equations to recursively obtain all the Haydock's coefficients and thus the macroscopic dielectric function.

A.1.4.2 Continued Fraction

To obtain a fast scheme to compute the continued fraction of Eq. (A.73) we use the following matrix multiplication,

$$\begin{pmatrix} p_n & p_{n-1} \\ q_n & q_{n-1} \end{pmatrix} = \begin{pmatrix} u-a_o & 1 \\ 1 & 0 \end{pmatrix} \begin{pmatrix} u-a_1 & 1 \\ -b_1^2 & 0 \end{pmatrix} \cdots \begin{pmatrix} u-a_n & 1 \\ -b_n^2 & 0 \end{pmatrix}, \tag{A.83}$$

from which it follows that

$$\frac{p_n}{q_n} = u - a_0 - \cfrac{b_1^2}{u - a_1 - \cfrac{b_2^2}{u-a_2-\cfrac{b_2^2}{\vdots}}}. \tag{A.84}$$

Then from Eq. (A.73) we obtain that

$$\epsilon^{M,LL} = \frac{\epsilon_a(\omega)}{u} \lim_{n\to\infty} \frac{p_n}{q_n}, \tag{A.85}$$

where in practice a large but finite n is needed to achieve convergence of the limit.

B Derivations for the transmission SHG yield in metamaterials

B.1 SHG for metamaterials

We know that the SHG yield is defined by

$$\mathcal{T}(2\omega) = \frac{I(2\omega)}{I(\omega)}, \tag{B.1}$$

with the intensity given by

$$I(\omega) = \frac{c}{2\pi} n(\omega) |E(\omega)|^2, \tag{B.2}$$

where $n(\omega) = [\epsilon(\omega)]^{1/2}$ is the refraction index with $\epsilon(\omega)$ as the dielectric function, and c the speed of light in vacuum.

As in Ref. [101], we assume a polarization sheet of the form of

$$\mathbf{P}(\mathbf{r}, t) = \boldsymbol{\mathcal{P}} e^{i\hat{\boldsymbol{\kappa}}\cdot\mathbf{R}} e^{-i\omega t} \delta(z - z_\beta) + c.c., \tag{B.3}$$

where $\mathbf{R} = (x, y)$, $\hat{\boldsymbol{\kappa}}$ is the component of the wave vector $\boldsymbol{\nu}_\beta$ parallel to the surface, z_β is the position of the sheet within the medium β, and $\boldsymbol{\mathcal{P}}$ is the position-independent polarization.

Ref. [102] demonstrate that the solution of Maxwell's equations for the radiated fields $E_{\beta,p\pm}$ and $E_{\beta,s}$ with $\mathbf{P}(\mathbf{r},t)$ as a source at points $z \neq 0$ can be written as

$$E_{\beta,s\pm} = \frac{2\pi i\tilde{\omega}^2}{\tilde{w_\beta}}\,\hat{\mathbf{s}}\cdot\boldsymbol{\mathcal{P}},$$
$$E_{\beta,p\pm} = \frac{2\pi i\tilde{\omega}^2}{\tilde{w_\beta}}\,\hat{\mathbf{p}}_{\beta,\pm}\cdot\boldsymbol{\mathcal{P}}, \tag{B.4}$$

where $\tilde{\omega} = \omega/c$. The supscripts $\pm$ are describing an upward $(+)$ or downward $(-)$ wave within the medium β. The vectors $\hat{\boldsymbol{s}}$ and $\hat{\boldsymbol{p}}_{\beta\pm}$ are the unit vectors for the s and p polarization of the radiated field. Also,

$$\hat{\boldsymbol{p}}_{\beta\pm} = \frac{\kappa(\omega)\hat{\boldsymbol{z}} \mp \tilde{w}_\beta(\omega)\hat{\boldsymbol{\kappa}}}{\tilde{\omega}n_\beta(\omega)} = \frac{\sin\theta_0\hat{\boldsymbol{z}} \mp w_\beta(\omega)\hat{\boldsymbol{\kappa}}}{n_\beta(\omega)}, \tag{B.5}$$

with

$$w_\beta = [\epsilon_\beta - \sin^2\theta_0]^{1/2}, \tag{B.6}$$

where θ_0 is the angle of incidence of the wave, $\kappa(\omega) = \tilde{\omega}\sin\theta_0$, $n_\beta(\omega) = [\epsilon_\beta(\omega)]^{1/2}$ is the refractive index of the medium β, and z is the direction perpendicular to the suface. For simplicity, we can consider the vector $\hat{\boldsymbol{\kappa}}$ in the x direction. If we consider the plane of incidence along the $\boldsymbol{\kappa}z$ plane, then

$$\hat{\boldsymbol{\kappa}} = \cos\phi\hat{\mathbf{x}} + \sin\phi\hat{\mathbf{y}} \tag{B.7}$$

and

$$\hat{\boldsymbol{s}} = \sin\phi\hat{\mathbf{x}} - \cos\phi\hat{\mathbf{y}} \tag{B.8}$$

where ϕ is the azimuthal angle with respect to the x axis. The nonlinear polarization is givne by

$$\boldsymbol{\mathcal{P}}_i = \chi^{(2)}_{ijk}(2\omega)E(\omega)_j E(\omega)_k, \tag{B.9}$$

where $\chi^{(2)}_{ijk}(2\omega)$ is the nonlinear susceptibility tensor. As in Ref. [101] we condider a polarization sheet oscillating at some frequency ω to express in a proper manner. We use ωexclusively to denote de fundamental frequency and $\hat{\boldsymbol{\kappa}}$ to denote de component of the incident wave vector parallel to the surface. The generated nonlinear polarization is oscillating at $\Omega = 2\omega$, and will be characterized by a wave vector parallel to the surface $\mathbf{K} = 2\kappa$. We can carry over Eqs. (B.4)-(B.7) simply y replacing the lowercase symbols $(\omega, \tilde{\omega}, \boldsymbol{\kappa}, n_\beta, \tilde{w}_\beta, w_\beta, \hat{\mathbf{p}}_{\beta\pm}, \hat{\mathbf{s}})$ with uppercase symbols $(\Omega, \tilde{\Omega}, \boldsymbol{K}, N_\beta, \tilde{W}_\beta, W_\beta, \hat{\mathbf{P}}_{\beta\pm}, \hat{\mathbf{S}})$, all evaluated at 2ω. Of course, we have $\hat{\mathbf{S}} = \hat{\mathbf{s}}$. We proceeded to analyze the radiated fields in transmission.

B.1.1 SHG radiated fields

Now, we are interesnting in calculate the fields due to a polarization sheet al $z = 0^+$ (see ref. [101]), where we are considering a SH field generated in the vacuum and it is propagated in de medium, then it is transmitted to the second vacuum region. In this way, we find the SH fiel radiated downward, is in the medium given by

$$\mathbf{E}^{2\omega}(\mathbf{r}) = \frac{2\pi i\tilde{\Omega}^2}{W_0}\mathbf{H}^m \cdot \boldsymbol{\mathcal{P}} e^{[i(Kx - Wz)]}, \tag{B.10}$$

where

$$\mathbf{H}^m = (\hat{\boldsymbol{S}} T^s_{0m} \hat{\boldsymbol{S}} + \hat{\boldsymbol{P}}_- T^p_{0m} \hat{\boldsymbol{P}}_{0-}), \tag{B.11}$$

with $W = [\epsilon(2\omega)\tilde{\Omega}^2 - K^2]^{1/2}$. The effects of the firts interface are describing by de Fresnel coefficients. As we say before, this field is propagated to the second interface and then cross back out to the vacuum. We express the output field at 2ω by

$$\mathbf{E}^{2\omega}_{out}(\mathbf{r}) = \frac{2\pi i\tilde{\Omega}^2}{W_0}\mathbf{H}^{m0} \cdot \boldsymbol{\mathcal{P}} (e^{[i(Kx + Wz)]} \times e^{[-iW_0(z+T)]}), \tag{B.12}$$

where

$$\mathbf{H}^{m0} = (\hat{\boldsymbol{S}} T^s_{0m} T^s_{m0} \hat{\boldsymbol{S}} + \hat{\boldsymbol{P}}_{0-} T^p_{0m} T^p_{m0} \hat{\boldsymbol{P}}_{0-}). \tag{B.13}$$

If we choose a specific polarization to detect denoted by $\hat{e}^{out}$, we get the amplitude

$$\begin{aligned} E_{out}^{2\omega} =& \frac{2\pi i\tilde{\Omega}^2}{W_0}\hat{e}^{out}\cdot\mathbf{H}^{m0}\cdot\boldsymbol{\mathcal{P}}e^{-[i(W_0-W)T]} \\ =& \frac{2\pi i\tilde{\Omega}^2}{W_0}\mathbf{e}^{2\omega}\cdot\boldsymbol{\mathcal{P}}e^{-[i(W_0-W)T]} \end{aligned} \tag{B.14}$$

where

$$\mathbf{e}^{2\omega} = \hat{e}^{out}\cdot\mathbf{H}^{m0}. \tag{B.15}$$

We can neglected the absortion of second harmonic field in the transversing slab, and finally obtain

$$I(2\omega) = \frac{32\pi^3\omega^2}{c^3}\sec\theta_0|\mathbf{e}^{2\omega,F}\cdot\boldsymbol{\chi}\mathbf{:}\mathbf{e}^{\omega,i}\mathbf{e}^{\omega,i}|^2 I^2(2\omega), \tag{B.16}$$

then, from Eq. (B.1) we obtain

$$\mathcal{T}_{iF} = \frac{32\pi^3\omega^2}{c^3}\sec\theta_0|\mathscr{T}_{iF}|^2 \tag{B.17}$$

where we have defined

$$\mathscr{T}_{iF} = \mathbf{e}^{2\omega,F}\cdot\boldsymbol{\chi}\mathbf{:}\mathbf{e}^{\omega,i}\mathbf{e}^{\omega,i}, \tag{B.18}$$

and the subscripts $i = s, p$ and $F = S, P$, were introduced to denote the direction of the incident field $\hat{\mathbf{e}}^{in}$, and the second harmonic field $\hat{\mathbf{e}}^{out}$ respectively. Now, we are able to calculate $\mathcal{T}_{iF}$ for the most common incoming and outcoming polarizations.

B.1.2 $\mathcal{T}_{pP}$ (p-in, P-out)

We start with the procedure to calculate $\mathcal{T}_{pP}$, it means we have the unit vector $\hat{e}^{in} = \hat{\mathbf{e}}^{p} = \hat{\mathbf{p}}_{0-}$ for the incoming field, and $\hat{e}^{out} = \hat{\mathbf{e}}^{P} = \hat{\mathbf{P}}_{0-}$ for the outcoming field. For that, it is needed to find the explicit expression $\mathscr{T}_{pP} = \mathbf{e}^{2\omega,P}\cdot\boldsymbol{\chi}\mathbf{:}\mathbf{e}^{\omega,p}\mathbf{e}^{\omega,p}$. We replace Eq. (B.13) into (B.15), we obtain

$$\mathbf{e}^{2\omega} = \hat{e}^{out}\cdot\mathbf{H}^{m0} = \hat{\boldsymbol{P}}_{0-}\cdot(\hat{\boldsymbol{S}}T^s_{0m}T^s_{m0}\hat{\boldsymbol{S}} + \hat{\boldsymbol{P}}_{0-}T^p_{0m}T^p_{m0}\hat{\boldsymbol{P}}_{0-}), \tag{B.19}$$

Table B.1: Fresnel Coefficients

At ω	At $\Omega = 2\omega$
$t^s_{ij} = \frac{2w_i}{w_i+w_j}$	$T^s_{ij} = \frac{2W_i}{W_i+W_j}$
$t^p_{ij} = \frac{2w_i[\epsilon_i(\omega)\epsilon_j(\omega)]^{1/2}}{w_i\epsilon_j(\omega)+w_j\epsilon_i(\omega)}$	$T^p_{ij} = \frac{2W_i[\epsilon_i(2\omega)\epsilon_j(2\omega)]^{1/2}}{W_i\epsilon_j(2\omega)+W_j\epsilon_i(2\omega)}$

where the Fresnel coeffcients for the transmission at are given in Table B.1.

In this way we obtain

$$T^s_{0m} = \frac{2W_0}{W_0 + W_m}, \qquad T^s_{m0} = \frac{2W_m}{W_m + W_0}, \tag{B.20}$$

for s polarization, and

$$T^p_{0m} = \frac{2W_0[N_0(2\omega)N_m(2\omega)]^{1/2}}{W_0N_m(2\omega) + W_mN_0(2\omega)}, \qquad T^p_{m0} = \frac{2W_m[N_m(2\omega)N_0(2\omega)]^{1/2}}{W_mN_0(2\omega) + W_0N_m(2\omega)}, \tag{B.21}$$

For this case by Eqs. (B.5) and (B.7)

$$\hat{\boldsymbol{P}}_{0-} = \frac{\sin\theta_0\hat{\boldsymbol{z}} + W_0\hat{\boldsymbol{\kappa}}}{N_0} = \sin\theta_0\hat{\boldsymbol{z}} + W_0\cos\phi\hat{\mathbf{x}} + W_0\sin\phi\hat{\mathbf{y}}. \tag{B.22}$$

Then for the second harmonic field

$$\begin{aligned}\mathbf{e}^{2\omega} &= \hat{\mathbf{e}}^{out} \cdot \left(\hat{\mathbf{S}} T^s_{0m} T^s_{0m} \hat{\mathbf{S}} + \hat{\mathbf{P}}_{0-} T^p_{0m} T^p_{m0} \hat{\mathbf{P}}_{0-} \right) \\ &= \hat{\mathbf{P}}_{0-} \cdot \left(\hat{\mathbf{S}} T^s_{0m} T^s_{0m} \hat{\mathbf{S}} + \hat{\mathbf{P}}_{0-} T^p_{0m} T^p_{m0} \hat{\mathbf{P}}_{0-} \right) \\ &= T^p_{0m} T^p_{m0} \hat{\mathbf{P}}_{0-},\end{aligned} \tag{B.23}$$

with Eq. (B.22)

$$\mathbf{e}^{2\omega} = \left(T^p_{0m} T^p_{m0} \right) \left(\sin\theta \hat{\mathbf{z}} + W_0 \cos\phi \hat{\mathbf{x}} + W_0 \sin\phi \hat{\mathbf{y}} \right). \tag{B.24}$$

For the incident fields

$$\begin{aligned}\mathbf{e}^{\omega} &= (\hat{\mathbf{s}} t^s_{0m} \hat{\mathbf{s}} + \hat{\mathbf{p}}_- t^p_{0m} \hat{\mathbf{p}}_{0-}) \cdot \hat{e}^{in} \\ &= (\hat{\mathbf{s}} t^s_{0m} \hat{\mathbf{s}} + \hat{\mathbf{p}}_- t^p_{0m} \hat{\mathbf{p}}_{0-}) \cdot \hat{\mathbf{p}}_{0-} \\ &= (\hat{\mathbf{p}}_- t^p_{0m} \hat{\mathbf{p}}_{0-}) \cdot \hat{\mathbf{p}}_{0-} = \hat{\mathbf{p}}_- t^p_{0m},\end{aligned} \tag{B.25}$$

and substituting Eq.(B.22) again, for $\hat{\mathbf{p}}_-$

$$\mathbf{e}^{\omega} = \left(\frac{t^p_{0m}}{n_m} \right) (\sin\theta \hat{\mathbf{z}} + w_m \cos\phi \hat{\mathbf{x}} + w_m \sin\phi \hat{\mathbf{y}}). \tag{B.26}$$

Taking the product between the two incident fields

$$\begin{aligned}\mathbf{e}^{\omega}\mathbf{e}^{\omega} = \left(\frac{t^p_{0m}}{n_m} \right)^2 \Big(& w_m^2 \cos^2\phi \hat{\mathbf{x}}\hat{\mathbf{x}} + 2w_m^2 \cos\phi \sin\phi \hat{\mathbf{x}}\hat{\mathbf{y}} \\ & + 2w_m \sin\theta \cos\phi \hat{\mathbf{x}}\hat{\mathbf{z}} + w_m^2 \sin^2\phi \hat{\mathbf{y}}\hat{\mathbf{y}} \\ & + 2w_m \sin\theta \sin\phi \hat{\mathbf{z}}\hat{\mathbf{y}} + \sin^2\theta \hat{\mathbf{z}}\hat{\mathbf{z}} \Big).\end{aligned} \tag{B.27}$$

With these expressions we can proceed to calculate

$$\begin{aligned}
\mathbf{e}^{2\omega}\cdot\chi^{s}\!:\!\mathbf{e}^{\omega}\mathbf{e}^{\omega} = \mathrm{T}_{pP}\Big[& W_0 w_m^2\cos^3\phi\chi_{xxx} \\
& + 2W_0 w_m^2\cos^2\phi\sin\phi\chi_{xxy} \\
& + 2W_0 w_m\sin\theta\cos^2\phi\chi_{xxz} \\
& + 2W_0 w_m^2\cos\phi\sin^2\phi\chi_{xyy} \\
& + 2W_0 w_m\sin\theta\cos\phi\sin\phi\chi_{xyz} \\
& + W_0\sin^2\theta\cos\phi\chi_{xzz} \\
& + W_0 w_m^2\cos^2\phi\sin\phi\chi_{yxx} \\
& + 2W_0 w_m^2\cos\phi\sin^2\phi\chi_{yxy} \\
& + 2W_0 w_m\sin\theta\cos\phi\sin\phi\chi_{yxz} \\
& + W_0 w_m^2\sin^3\phi\chi_{yyy} \\
& + 2W_0 w_m\sin\theta\sin^2\phi\chi_{yyz} \\
& + W_0\sin^2\theta\sin\phi\chi_{yzz} \\
& + w_m^2\sin\theta\cos^2\phi\chi_{zxx} \\
& + 2w_m\sin^2\theta\cos\phi\chi_{zxz} \\
& + 2w_m^2\sin\theta\cos\phi\sin\phi\chi_{zxy} \\
& + w_m^2\sin\theta\sin^2\phi\chi_{zyy} \\
& + 2w_m\sin^2\theta\sin\phi\chi_{zzy} \\
& + \sin^3\theta\chi_{zzz}\Big],
\end{aligned} \tag{B.28}$$

where

$$\mathrm{T}_{pP} = \left(T_{0m}^{p}T_{m0}^{p}\right)\left(\frac{t_{0m}^{p}}{n_m}\right)^2. \tag{B.29}$$

Considering the symmetry of the metamaterial, we have that the only non-zero compo-

nents of χ_{ijk} are χ_{xxy}, χ_{yxx} and χ_{yyy}, then Eq.(B.28) is reduced to

$$\mathscr{T}_{pP} = W_0 w_m^2 \mathrm{T}_{pP}\Big[2\cos^2\phi\sin\phi\chi_{xxy} + \cos^2\phi\sin\phi\chi_{yxx} + \sin^3\phi\chi_{yyy}\Big], \tag{B.30}$$

and after some algebra

$$\begin{aligned}\mathscr{T}_{pP} = \frac{W_0 w_m^2}{2}\mathrm{T}_{pP}\Big[&\sin\phi\Big(\chi_{xxy} + \chi_{yxx} + \frac{\chi_{yyy}}{2}\Big)\\ &+ \sin 3\phi\Big(\chi_{xxy} + \chi_{yxx} - \frac{\chi_{yyy}}{2}\Big)\Big].\end{aligned} \tag{B.31}$$

$$\begin{aligned}\mathscr{T}_{pP} = \frac{W_0 w_m^2}{4}\mathrm{T}_{pP}\Big[&\sin\phi\Big(2\chi_{xxy} + \chi_{yxx} + 3\chi_{yyy}\Big)\\ &+ \sin 3\phi\Big(2\chi_{xxy} + \chi_{yxx} - \chi_{yyy}\Big)\Big].\end{aligned} \tag{B.32}$$

B.1.3 $\mathcal{T}_{pS}$ (p-in, S-out)

Now, we follow the same procedure as before, where now, we want to calculate $\mathcal{T}_{pS}$, with $\hat{e}^{in} = \hat{\mathbf{e}}^p = \hat{\mathbf{p}}_{0-}$ for the incoming field, and $\hat{e}^{out} = \hat{\mathbf{e}}^S = \hat{\mathbf{S}}$ for the outcoming field. It is needed to find the explicit expression $\mathscr{T}_{pP} = \mathbf{e}^{2\omega,S}\cdot\boldsymbol{\chi}:\mathbf{e}^{\omega,p}\mathbf{e}^{\omega,p}$. We replace Eq. (B.13) into (B.15) again, and obtain

$$\mathbf{e}^{2\omega} = \hat{e}^{out}\cdot\mathbf{H}^{m0} = \hat{\boldsymbol{S}}\cdot(\hat{\boldsymbol{S}}T^s_{0m}T^s_{m0}\hat{\boldsymbol{S}} + \hat{\boldsymbol{P}}_{0-}T^p_{0m}T^p_{m0}\hat{\boldsymbol{P}}_{0-}), \tag{B.33}$$

where the Fresnel coefficients for the transmission at are given in Table B.1. We have for the second harmonic field

$$\begin{aligned}\mathbf{e}^{2\omega} &= \hat{\mathbf{e}}^{out}\cdot\left(\hat{\mathbf{S}}T^s_{0m}T^s_{0m}\hat{\mathbf{S}} + \hat{\mathbf{P}}_{0-}T^p_{0m}T^p_{m0}\hat{\mathbf{P}}_{0-}\right)\\ &= \hat{\mathbf{S}}\cdot\left(\hat{\mathbf{S}}T^s_{0m}T^s_{0m}\hat{\mathbf{S}} + \hat{\mathbf{P}}_{0-}T^p_{0m}T^p_{m0}\hat{\mathbf{P}}_{0-}\right)\\ &= T^s_{0m}T^s_{m0}\hat{\mathbf{S}}\end{aligned} \tag{B.34}$$

Using Eq. (B.8),

$$\mathbf{e}^{2\omega} = \left(T^s_{0m}T^s_{m0}\right)\left(\sin\phi\hat{\mathbf{x}} - \cos\phi\hat{\mathbf{y}}\right). \tag{B.35}$$

Now, for the incident fields

$$\begin{aligned}\mathbf{e}^{\omega} &= (\hat{\mathbf{s}}t^s_{0m}\hat{\mathbf{s}} + \hat{\mathbf{p}}_- t^p_{0m}\hat{\mathbf{p}}_{0-})\cdot\hat{\mathbf{e}}^{in}\\ &= (\hat{\mathbf{s}}t^s_{0m}\hat{\mathbf{s}} + \hat{\mathbf{p}}_- t^p_{0m}\hat{\mathbf{p}}_{0-})\cdot\hat{\mathbf{p}}_{0-}\\ &= (\hat{\mathbf{p}}_- t^p_{0m}\hat{\mathbf{p}}_{0-})\cdot\hat{\mathbf{p}}_{0-} = \hat{\mathbf{p}}_- t^p_{0m},\end{aligned} \tag{B.36}$$

with Eq.(B.22), we actually recover Eq.(B.56) and Eq.(B.22), for the incident fields and their product. With these expressions we calculate

$$\begin{aligned}\mathbf{e}^{2\omega}\cdot\chi^s{:}\mathbf{e}^{\omega}\mathbf{e}^{\omega} = \mathrm{T}_{pS}\Big[&w_m^2\cos^2\phi\sin\phi\chi_{xxx}\\ &+ 2w_m^2\cos\phi\sin^2\phi\chi_{xxy}\\ &+ 2w_m\sin\theta\cos\phi\sin\phi\chi_{xxz}\\ &+ w_m^2\sin^3\phi\chi_{xyy}\\ &+ 2w_m\sin\theta\sin^2\phi\chi_{xyz}\\ &+ \sin^2\theta\sin\phi\chi_{xzz}\\ &- w_m^2\cos^3\phi\chi_{yxx}\\ &- 2w_m^2\cos^2\phi\sin\phi\chi_{yxy}\\ &- 2w_m\sin\theta\cos^2\phi\chi_{yxz}\\ &- w_m^2\cos\phi\sin^2\phi\chi_{yyy}\\ &- 2w_m\sin\theta\cos\phi\sin\phi\chi_{yyz}\\ &- \sin^2\theta\cos\phi\chi_{yzz}\Big],\end{aligned} \tag{B.37}$$

where,

$$\mathrm{T}_{pS} = \left(T^s_{0m}T^s_{m0}\right)\left(\frac{t^p_{0m}}{n_m}\right)^2. \tag{B.38}$$

As in the previous section, we only consider the non-zero components of χ_{ijk}, they are χ_{xxy}, χ_{yxx} and χ_{yyy}, then Eq.(B.37) is reduced to

$$\mathscr{T}_{pS} = w_m^2 \mathrm{T}_{pS}\Big[2\cos\phi\sin^2\phi\chi_{xxy} - \cos^3\phi\chi_{yxx} - \cos\phi\sin^2\phi\chi_{yyy}\Big], \tag{B.39}$$

and after some algebra, we obtain

$$\begin{aligned}\mathscr{T}_{pS} = \frac{w_m^2}{4}\mathrm{T}_{pS}\Big[&\cos\phi\Big(2\chi_{xxy} - \chi_{yyy} - 3\chi_{yxx}\Big)\\ &+ \cos 3\phi\Big(\chi_{yyy} - 2\chi_{xxy} - \chi_{yxx}\Big)\Big].\end{aligned} \tag{B.40}$$

B.1.4 $\mathcal{T}_{sS}$ (s-in, S-out)

Now, we follow the same procedure as before, where now, we want to calculate $\mathcal{T}_{sS}$, with $\hat{e}^{in} = \hat{\mathbf{e}}^s = \hat{\mathbf{s}}$ for the incoming field, and $\hat{e}^{out} = \hat{\mathbf{e}}^S = \hat{\mathbf{S}}$ for the outcoming field. It is needed to find the explicit expression $\mathscr{T}_{sS} = \mathbf{e}^{2\omega,S}\cdot\boldsymbol{\chi}:\mathbf{e}^{\omega,s}\mathbf{e}^{\omega,s}$. We replace Eq. (B.13) into (B.15) again, and obtain

$$\mathbf{e}^{2\omega} = \hat{e}^{out}\cdot\mathbf{H}^{m0} = \hat{\boldsymbol{S}}\cdot(\hat{\boldsymbol{S}}T^s_{0m}T^s_{m0}\hat{\boldsymbol{S}} + \hat{\boldsymbol{P}}_{0-}T^p_{0m}T^p_{m0}\hat{\boldsymbol{P}}_{0-}), \tag{B.41}$$

where the Fresnel coefficients for the transmission at are given in Table B.1. We have for the second harmonic field

$$\begin{aligned}\mathbf{e}^{2\omega} &= \hat{\mathbf{e}}^{out}\cdot\left(\hat{\mathbf{S}}T^s_{0m}T^s_{0m}\hat{\mathbf{S}} + \hat{\mathbf{P}}_{0-}T^p_{0m}T^p_{m0}\hat{\mathbf{P}}_{0-}\right)\\ &= \hat{\mathbf{S}}\cdot\left(\hat{\mathbf{S}}T^s_{0m}T^s_{0m}\hat{\mathbf{S}} + \hat{\mathbf{P}}_{0-}T^p_{0m}T^p_{m0}\hat{\mathbf{P}}_{0-}\right)\\ &= T^s_{0m}T^s_{m0}\hat{\mathbf{S}}.\end{aligned} \tag{B.42}$$

Using Eq. (B.8),

$$\mathbf{e}^{2\omega} = \left(T^s_{0m}T^s_{m0}\right)\left(\sin\phi\hat{\mathbf{x}} - \cos\phi\hat{\mathbf{y}}\right). \tag{B.43}$$

Now, for the incoming fields

$$\begin{aligned}\mathbf{e}^{\omega} &= (\hat{\mathbf{s}}t^{s}_{0m}\hat{\mathbf{s}} + \hat{\mathbf{p}}_{-}t^{p}_{0m}\hat{\mathbf{p}}_{0-}) \cdot \hat{\mathbf{e}}^{in} \\ &= (\hat{\mathbf{s}}t^{s}_{0m}\hat{\mathbf{s}} + \hat{\mathbf{p}}_{-}t^{p}_{0m}\hat{\mathbf{p}}_{0-}) \cdot \hat{\mathbf{s}} \\ &= (\hat{\mathbf{s}}t^{s}_{0m}\hat{\mathbf{s}}) \cdot \hat{\mathbf{s}} = \hat{\mathbf{s}}t^{s}_{0m},\end{aligned} \tag{B.44}$$

and using Eq. (B.8) again, we obtain

$$\mathbf{e}^{\omega} = \left(t^{s}_{0m}\right)\left(\sin\phi\hat{\mathbf{x}} - \cos\phi\hat{\mathbf{y}}\right), \tag{B.45}$$

and the product of the incident fields

$$\mathbf{e}^{\omega}\mathbf{e}^{\omega} = \left(t^{s}_{0m}\right)^{2}\left(\sin^{2}\phi\hat{\mathbf{x}}\hat{\mathbf{x}} - 2\sin\phi\cos\phi\hat{\mathbf{x}}\hat{\mathbf{y}} + \cos^{2}\phi\hat{\mathbf{y}}\hat{\mathbf{y}}\right). \tag{B.46}$$

With these expressions we calculate

$$\begin{aligned}\mathbf{e}^{2\omega}\cdot\chi^{s}\!:\!\mathbf{e}^{\omega}\mathbf{e}^{\omega} = \mathrm{T}_{sS}\Big[&\sin^{3}\phi\chi_{xxx} \\ &- 2\sin^{2}\phi\cos\phi\chi_{xxy} \\ &+ \sin\phi\cos^{2}\phi\chi_{xyy} \\ &- \sin^{2}\phi\cos\phi\chi_{yxx} \\ &+ 2\sin\phi\cos^{2}\phi\chi_{yxy} \\ &- \cos^{3}\phi\chi_{yyy}\Big],\end{aligned} \tag{B.47}$$

where,

$$\mathrm{T}_{sS} = \left(T^{s}_{0m}T^{s}_{m0}\right)\left(t^{s}_{0m}\right)^{2}. \tag{B.48}$$

Considering the non-zero components of χ_{ijk}, they are χ_{xxy}, χ_{yxx} and χ_{yyy}, then Eq.(B.47) is reduced to

$$\mathscr{T}_{sS} = \mathrm{T}_{sS}\Big[-2\sin^{2}\phi\cos\phi\chi_{xxy} - \sin^{2}\phi\cos\phi\chi_{yxx} - \cos^{3}\phi\chi_{yyy}\Big], \tag{B.49}$$

and after some algebra, we obtain

$$\mathscr{T}_{sS} = \frac{\mathrm{T}_{sS}}{4}\left[\cos 3\phi\Big(2\chi_{xxy} + \chi_{yxx} - \chi_{yyy}\Big) - \cos\phi\Big(2\chi_{xxy} + \chi_{yxx} + 3\chi_{yyy}\Big)\right], \quad \text{(B.50)}$$

B.1.5 $\mathcal{T}_{sP}$ (s-in, P-out)

Now, we follow the same procedure as before, where now, we want to calculate $\mathcal{T}_{sP}$, with $\hat{e}^{in} = \hat{\mathbf{e}}^{s} = \hat{\mathbf{s}}$ for the incoming field, and $\hat{e}^{out} = \hat{\mathbf{e}}^{P} = \hat{\mathbf{P}}_{0-}$ for the outcoming field. It is needed to find the explicit expression $\mathscr{T}_{sP} = \mathbf{e}^{2\omega,p}\cdot\boldsymbol{\chi}\!:\!\mathbf{e}^{\omega,s}\mathbf{e}^{\omega,s}$. We replace Eq. (B.13) into (B.15) again, and obtain

$$\mathbf{e}^{2\omega} = \hat{e}^{out}\cdot\mathbf{H}^{m0} = \hat{\boldsymbol{P}}_{0-}\cdot(\hat{\boldsymbol{S}}T^{s}_{0m}T^{s}_{m0}\hat{\boldsymbol{S}} + \hat{\boldsymbol{P}}_{0-}T^{p}_{0m}T^{p}_{m0}\hat{\boldsymbol{P}}_{0-}), \quad \text{(B.51)}$$

where the Fresnel coefficients for the transmission at are given in Table B.1. We have for the second harmonic field

$$\begin{aligned}\mathbf{e}^{2\omega} &= \hat{\mathbf{e}}^{out}\cdot\left(\hat{\mathbf{S}}T^{s}_{0m}T^{s}_{0m}\hat{\mathbf{S}} + \hat{\mathbf{P}}_{0-}T^{p}_{0m}T^{p}_{m0}\hat{\mathbf{P}}_{0-}\right)\\ &= \hat{\mathbf{P}}_{0-}\cdot\left(\hat{\mathbf{S}}T^{s}_{0m}T^{s}_{0m}\hat{\mathbf{S}} + \hat{\mathbf{P}}_{0-}T^{p}_{0m}T^{p}_{m0}\hat{\mathbf{P}}_{0-}\right)\\ &= T^{p}_{0m}T^{p}_{m0}\hat{\mathbf{P}}_{0-},\end{aligned} \quad \text{(B.52)}$$

with Eq. (B.22)

$$\mathbf{e}^{2\omega} = \left(T^{p}_{0m}T^{p}_{m0}\right)\left(\sin\theta\hat{\mathbf{z}} + W_0\cos\phi\hat{\mathbf{x}} + W_0\sin\phi\hat{\mathbf{y}}\right). \quad \text{(B.53)}$$

For the incident fields

$$\begin{aligned}\mathbf{e}^{\omega} &= (\hat{\mathbf{s}}t^{s}_{0m}\hat{\mathbf{s}} + \hat{\mathbf{p}}_{-}t^{p}_{0m}\hat{\mathbf{p}}_{0-})\cdot\hat{\mathbf{e}}^{in}\\ &= (\hat{\mathbf{s}}t^{s}_{0m}\hat{\mathbf{s}} + \hat{\mathbf{p}}_{-}t^{p}_{0m}\hat{\mathbf{p}}_{0-})\cdot\hat{\mathbf{s}}\\ &= (\hat{\mathbf{s}}t^{s}_{0m}\hat{\mathbf{s}})\cdot\hat{\mathbf{s}} = \hat{\mathbf{s}}t^{s}_{0m},\end{aligned} \quad \text{(B.54)}$$

and using Eq. (B.8) again, we obtain

$$\mathbf{e}^{\omega} = \left(t^{s}_{0m}\right)\left(\sin\phi\hat{\mathbf{x}} - \cos\phi\hat{\mathbf{y}}\right), \tag{B.55}$$

and the product of the incident fields

$$\mathbf{e}^{\omega}\mathbf{e}^{\omega} = \left(t^{s}_{0m}\right)^{2}\left(\sin^{2}\phi\hat{\mathbf{x}}\hat{\mathbf{x}} - 2\sin\phi\cos\phi\hat{\mathbf{x}}\hat{\mathbf{y}} + \cos^{2}\phi\hat{\mathbf{y}}\hat{\mathbf{y}}\right). \tag{B.56}$$

With these expressions we calculate

$$\begin{aligned}\mathbf{e}^{2\omega}\cdot\chi^{s}\!:\!\mathbf{e}^{\omega}\mathbf{e}^{\omega} = \mathrm{T}_{sP}\Big[& W_0\cos\phi\sin^{2}\phi\chi_{xxx} \\ & - 2W_0\cos^{2}\phi\sin\phi\chi_{xxy} \\ & + W_0\cos^{3}\phi\chi_{xyy} \\ & + W_0\sin^{3}\phi\chi_{yxx} \\ & - 2W_0\cos\phi\sin^{2}\phi\chi_{yxy} \\ & + W_0\cos^{2}\phi\sin\phi\chi_{yyy} \\ & + \sin\theta\sin^{2}\phi\chi_{zxx} \\ & - 2\sin\theta\cos\phi\sin\phi\chi_{zxy} \\ & + \sin\theta\cos^{2}\phi\chi_{zyy}\Big].\end{aligned} \tag{B.57}$$

Where,

$$\mathrm{T}_{sP} = \left(T^{p}_{0m}T^{p}_{m0}\right)\left(t^{s}_{0m}\right)^{2} \tag{B.58}$$

Considering the non-zero components of χ_{ijk}, they are χ_{xxy}, χ_{yxx} and χ_{yyy}, then Eq.(B.57) is reduced to

$$\mathscr{T}_{sP} = \mathrm{T}_{sP}\Big[-2W_0\cos^{2}\phi\sin\phi\chi_{xxy} + W_0\sin^{3}\phi\chi_{yxx} + W_0\cos^{2}\phi\sin\phi\chi_{yyy}\Big], \tag{B.59}$$

and after some algebra, we obtain

$$\mathscr{T}_{sP} = \frac{W_0}{4}\mathrm{T}_{sP}\Bigg[\sin\phi\Big(\chi_{yyy} - 2\chi_{xxy} + 3\chi_{yxx}\Big) + \sin 3\phi\Big(\chi_{yyy} - 2\chi_{xxy} - \chi_{yxx}\Big)\Bigg], \tag{B.60}$$

C Achievements of the Thesis: Articles and Conferences

As part of this thesis the following achievement are noted

1. **Articles**

   - **Second-harmonic generation in nanostructured metamaterials**,
     Ulises R. Meza and Bernardo S. Mendoza and W. Luis Mochán,
     Physical Review B **99**, 125408 (2019).
     DOI: https://doi.org/10.1103/PhysRevB.99.125408
   - **Metamateriales nanoestructurados: avances en el cálculo de sus propiedades ópticas**
     Ulises R. Meza, Bernardo S. Mendoza, W. L. Mochán,
     Mundo Nano: Artículos de Revisión, **13** (24), 1e-18e, enero–junio 2020.
     DOI: https://doi.org/10.22201/ceiich.24485691e.2020.24.69611

2. **Conferences**

   - **APS March Meeting 2021**, Oral presentation, USA, 2021
   - **Siegman International School on Lasers**, Poster presentation, USA, 2019

- **The International Conference on Optics of Surfaces and Interfaces (OSI 13)**, Poster presentation, Mexico, 2019
- **Symposium of Nanoscience and Nanomaterials**, Oral presentation, Mexico, 2019
- **Escuela Latinoamericana Óptica (ELO-2018)**,Oral presentation, Mexico, 2018
- **SMF Reunión Anual de la División de Estado Sólido**, Poster presentation, Mexico, 2018

Bibliography

[1] A. Femius Koenderink, Andrea Alù, and Albert Polman. Nanophotonics: Shrinking light-based technology. *Science*, 348(6234):516–521, 2015. Publisher: American Association for the Advancement of Science.

[2] Dong Zhao, Zhelin Lin, Wenqi Zhu, Henri J. Lezec, Ting Xu, Amit Agrawal, Cheng Zhang, and Kun Huang. Recent advances in ultraviolet nanophotonics: from plasmonics and metamaterials to metasurfaces. *Nanophotonics*, 10(9):2283–2308, 2021. Publisher: De Gruyter.

[3] Francesco Monticone and Andrea Alù. Metamaterial, plasmonic and nanophotonic devices. *Reports on Progress in Physics*, 80(3):036401, 2017.

[4] Wenshan Cai and Vladimir Shalaev. *Optical Metamaterials*. Springer New York, 2010.

[5] Adnan Ali, Anirban Mitra, and Brahim Aïssa. Metamaterials and metasurfaces: A review from the perspectives of materials, mechanisms and advanced metadevices. *Nanomaterials*, 12(6):1027, 2022. Number: 6 Publisher: Multidisciplinary Digital Publishing Institute.

[6] Yongmin Liu and Xiang Zhang. Metamaterials: a new frontier of science and technology. *Chem. Soc. Rev.*, 40(5):2494–2507, 2011. Publisher: The Royal Society of Chemistry.

[7] Abhijit Biswas, Ilker S. Bayer, Alexandru S. Biris, Tao Wang, Enkeleda Dervishi, and Franz Faupel. Advances in top–down and bottom–up surface nanofabrication: Techniques, applications & future prospects. *Advances in Colloid and Interface Science*, 170(1):2–27, 2012.

[8] Tiziana Cesca, Niccolò Michieli, Boris Kalinic, Ana Sánchez-Espinoza, Marco Rattin, Valentina Russo, Valentina Mattarello, Carlo Scian, Paolo Mazzoldi, and Giovanni Mattei. Nonlinear absorption tuning by composition control in bimetallic plasmonic nanoprism arrays. *Nanoscale*, 7:12411–12418, 2015.

[9] Yifang Chen. Nanofabrication by electron beam lithography and its applications: A review. *Microelectronic Engineering*, 135:57–72, 2015.

[10] Priscila Romagnoli, Maki Maeda, Jonathan M. Ward, Viet Giang Truong, and Síle Nic Chormaic. Fabrication of optical nanofibre-based cavities using focussed ion-beam milling: a review. *Applied Physics B*, 126(6):111, 2020.

[11] Zeinab Chehadi, Michele Montanari, Nicoletta Granchi, Mehrnaz Modaresialam, Mathieu Koudia, Mathieu Abel, Magali Putero, David Grosso, Francesca Intonti, and Marco Abbarchi. Soft nano-imprint lithography of rare-earth-doped light-emitting photonic metasurface. *Advanced Optical Materials*, n/a:2201618, 2022. _eprint: https://onlinelibrary.wiley.com/doi/pdf/10.1002/adom.202201618.

[12] Tengfei Qiu, Eser Metin Akinoglu, Bin Luo, Muxina Konarova, Jung-Ho Yun, Ian R. Gentle, and Lianzhou Wang. Nanosphere lithography: A versatile approach

to develop transparent conductive films for optoelectronic applications. *Advanced Materials*, 34(19):2103842, 2022.

[13] Muamer Kadic, Graeme W. Milton, Martin van Hecke, and Martin Wegener. 3d metamaterials. *Nature Review Physics*, 1(3):198–210, 2019.

[14] Viktor G. Veselago. The electrodynamics of substances with simultaneously negative values of ϵ and μ. *Soviet Physics Uspekhi*, 10(4):509, 1968.

[15] John Brian Pendry. Negative refraction makes a perfect lens. *Physical Review Letters*, 85(18):3966, 2000.

[16] David R Smith, Willie J Padilla, DC Vier, Syrus C Nemat-Nasser, and Seldon Schultz. Composite medium with simultaneously negative permeability and permittivity. *Physical Review Letters*, 84(18):4184, 2000.

[17] Vladimir M. Shalaev, Wenshan Cai, Uday K. Chettiar, Hsiao-Kuan Yuan, Andrey K. Sarychev, Vladimir P. Drachev, and Alexander V. Kildishev. Negative index of refraction in optical metamaterials. *Opt. Lett.*, 30(24):3356–3358, Dec 2005.

[18] Alexander V. Kildishev, Wenshan Cai, Uday K. Chettiar, Hsiao-Kuan Yuan, Andrey K. Sarychev, Vladimir P. Drachev, and Vladimir M. Shalaev. Negative refractive index in optics of metal-dielectric composites. *J. Opt. Soc. Am. B*, 23(3):423–433, Mar 2006.

[19] John B Pendry, David Schurig, and David R Smith. Controlling electromagnetic fields. *Science*, 312(5781):1780–1782, 2006.

[20] Ulf Leonhardt. Optical conformal mapping. *Science*, 312(5781):1777–1780, 2006.

[21] Jiaming Hao, Wei Yan, and Min Qiu. Super-reflection and cloaking based on zero index metamaterial. *Applied Physics Letters*, 96(10):101109, 2010.

[22] Simin Feng and Klaus Halterman. Parametrically shielding electromagnetic fields by nonlinear metamaterials. *Physical Review Letters*, 100(6):063901, 2008.

[23] Leonid V Alekseyev, Viktor A Podolskiy, and Evgenii E Narimanov. Homogeneous hyperbolic systems for terahertz and far-infrared frequencies. *Advances in OptoElectronics*, 2012, 2012.

[24] Norman Born, Ralf Gente, I Al-Naib, and Martin Koch. Laser beam machined free-standing terahertz metamaterials. *Electronics Letters*, 51(13):1012–1014, 2015.

[25] Takehito Suzuki, Masashi Sekiya, Tatsuya Sato, and Yuki Takebayashi. Negative refractive index metamaterial with high transmission, low reflection, and low loss in the terahertz waveband. *Optics Express*, 26(7):8314–8324, 2018.

[26] Mikhail Lapine, Ilya V. Shadrivov, and Yuri S. Kivshar. Colloquium: Nonlinear metamaterials. *Reviews of Modern Physics*, 86(3):1093–1123, 2014. Publisher: American Physical Society.

[27] Sean P. Rodrigues, Preston A. Cunha, Kaushik Kudtarkar, Ercan M. Dede, and Shoufeng Lan. Review of optically active and nonlinear chiral metamaterials. *Journal of Nanophotonics*, 16(2):020901, 2022. Publisher: SPIE.

[28] Natalia M. Litchinitser. Nonlinear optics in metamaterials. *Advances in Physics: X*, 3(1):1367628, 2018.

[29] Kebin Fan, Richard D. Averitt, and Willie J. Padilla. Active and tunable nanophotonic metamaterials. *Nanophotonics*, 11(17):3769–3803, 2022. Publisher: De Gruyter.

[30] Yun Zhao, Yuanmu Yang, and Hong-Bo Sun. Nonlinear meta-optics towards applications. *PhotoniX*, 2(1):3, 2021.

[31] Stéphane Larouche and David R Smith. A retrieval method for nonlinear metamaterials. *Optics Communications*, 283(8):1621–1627, 2010.

[32] Kevin O'Brien, Haim Suchowski, Junsuk Rho, Alessandro Salandrino, Boubacar Kante, Xiaobo Yin, and Xiang Zhang. Predicting nonlinear properties of metamaterials from the linear response. *Nature Materials*, 14(4):379, 2015.

[33] Stéphane Larouche and Vesna Radisic. Retrieval of all effective susceptibilities in nonlinear metamaterials. *Physical Review A*, 97(4):043863, 2018.

[34] Ilya V Shadrivov, Alexander A Zharov, and Yuri S Kivshar. Second-harmonic generation in nonlinear left-handed metamaterials. *JOSA B*, 23(3):529–534, 2006.

[35] Hannu Husu, Roope Siikanen, Jouni Makitalo, Joonas Lehtolahti, Janne Laukkanen, Markku Kuittinen, and Martti Kauranen. Metamaterials with tailored nonlinear optical response. *Nano Letters*, 12(2):673–677, 2012.

[36] Alexander A Zharov, Ilya V Shadrivov, and Yuri S Kivshar. Nonlinear properties of left-handed metamaterials. *Physical Review Letters*, 91(3):037401, 2003.

[37] Matthias W. Klein, Christian Enkrich, Martin Wegener, and Stefan Linden. Second-harmonic generation from magnetic metamaterials. *Science (New York, N.Y.)*, 313(5786):502–504, 2006.

[38] Giuseppe Marino, Paulina Segovia, Alexey V Krasavin, Pavel Ginzburg, Nicolas Olivier, Gregory A Wurtz, and Anatoly V Zayats. Second-harmonic generation from hyperbolic plasmonic nanorod metamaterial slab. *Laser & Photonics Reviews*, 12(2):1700189, 2018.

[39] Brian K Canfield, Hannu Husu, Janne Laukkanen, Benfeng Bai, Markku Kuittinen, Jari Turunen, and Martti Kauranen. Local field asymmetry drives second-harmonic generation in noncentrosymmetric nanodimers. *Nano Letters*, 7(5):1251–1255, 2007.

[40] Pai-Yen Chen, Christos Argyropoulos, and Andrea Alù. Enhanced nonlinearities using plasmonic nanoantennas. *Nanophotonics*, 1(3-4):221–233, 2012.

[41] Daniel Timbrell, Jian Wei You, Yuri S Kivshar, and Nicolae C Panoiu. A comparative analysis of surface and bulk contributions to second-harmonic generation in centrosymmetric nanoparticles. *Scientific Reports*, 8(1):3586, 2018.

[42] Jonathan Bar-David and Uriel Levy. Second harmonic generation in geometric-phase resonant dielectric metasurfaces. In *CLEO: Science and Innovations*, pages JW2A–98. Optical Society of America, 2018.

[43] Matan Galanty, Omer Shavit, Adam Weissman, Hannah Aharon, David Gachet, Elad Segal, and Adi Salomon. Second harmonic generation hotspot on a centrosymmetric smooth silver surface. *Light: Science & Applications*, 7(1):49, 2018.

[44] Tsafrir Abir, Mai Tal, and Tal Ellenbogen. Second-harmonic enhancement from a nonlinear plasmonic metasurface coupled to an optical waveguide. *Nano Letters*, 22(7):2712–2717, 2022. Publisher: American Chemical Society.

[45] Martti Kauranen and Anatoly V. Zayats. Nonlinear plasmonics. *Nature Photonics*, 6(11):737–748, 2012.

[46] P.A. Franken, A.E. Hill, C.W. Peters, and G. Weinreich. Generation of optical harmonics. *Physical Review Letters*, 7(4):118–119, 1961.

[47] M. A. Yurkin and A. G. Hoekstra. The discrete dipole approximation: An overview and recent developments. *Journal of Quantitative Spectroscopy and Radiative Transfer*, 106(1):558–589, 2007.

[48] Diogo F. Carvalho, Manuel A. Martins, Paulo A. Fernandes, and M. Rosário P. Correia. Coupling of plasmonic nanoparticles on a semiconductor substrate via a modified discrete dipole approximation method. *Phys. Chem. Chem. Phys.*, pages –, 2022.

[49] Constantin R Simovski. On electromagnetic characterization and homogenization of nanostructured metamaterials. *Journal of Optics*, 13(1):013001, 2010.

[50] Andrea Alu. First-principles homogenization theory for periodic metamaterials. *Physical Review B*, 84(7):075153, 2011.

[51] W. Luis Mochán and Rubén G. Barrera. Electromagnetic response of systems with spatial fluctuations I. general formalism. *Physical Review B*, 32(8):4984–4988, 1985.

[52] W. Luis Mochán and Rubén G. Barrera. Electromagnetic response of systems with spatial fluctuations II. applications. *Physical Review B*, 32(8):4989–5001, 1985.

[53] Ernesto Cortes, Luis Mochán, Bernardo S Mendoza, and Guillermo P Ortiz. Optical properties of nanostructured metamaterials. *Physica Status Solidi (b)*, 247(8):2102–2107, 2010.

[54] W Luis Mochán, Guillermo P Ortiz, and Bernardo S Mendoza. Efficient homogenization procedure for the calculation of optical properties of 3d nanostructured composites. *Optics Express*, 18(21):22119–22127, 2010.

[55] JS Pérez-Huerta, Guillermo P Ortiz, Bernardo S Mendoza, and W Luis Mochan. Macroscopic optical response and photonic bands. *New Journal of Physics*, 15(4):043037, 2013.

[56] W Luis Mochán, Bernardo S Mendoza, and Irina Solís. Second harmonic generation in nanostructured metamaterials. In *Latin America Optics and Photonics Conference*, pages LM2C–2. Optical Society of America, 2014.

[57] Bernardo S Mendoza and W Luis Mochán. Tailored optical polarization in nanostructured metamaterials. *Physical Review B*, 94(19):195137, 2016.

[58] Photonic - A perl package for calculations on photonics and metamaterials v0.010. https://metacpan.org/pod/Photonic, 2018.

[59] Roger Haydock. The recursive solution of the schrodinger equation. In *Solid State Physics*, volume 35, pages 215–294. Elsevier, 1980.

[60] Ulises R. Meza, Bernardo S. Mendoza, and W. Luis Mochán. Second-harmonic generation in nanostructured metamaterials. *Physical Review B*, 99(12), 2019.

[61] James C Garland and David Burnham Tanner. Electrical transport and optical properties of inhomogeneous media. Technical report, American Institute of Physics, New York, 1978.

[62] D. R. Smith, J. B. Pendry, and M. C. K. Wiltshire. Metamaterials and negative refractive index. *Science*, 305(5685):788–792, August 2004.

[63] Yoshihiro Akahane, Takashi Asano, Bong-Shik Song, and Susumu Noda. High-q photonic nanocavity in a two-dimensional photonic crystal. *Nature*, 425(6961):944, 2003.

[64] AN Grigorenko, AK Geim, HF Gleeson, Ying Zhang, AA Firsov, IY Khrushchev, and J Petrovic. Nanofabricated media with negative permeability at visible frequencies. *Nature*, 438(7066):335, 2005.

[65] Soner Balci, David A Czaplewski, Il Woong Jung, Ju-Hyung Kim, Fariba Hatami, Patrick Kung, and Seongsin Margaret Kim. High efficient thz emission from unbiased and biased semiconductor nanowires fabricated using electron beam lithography. *IEEE Journal of Selected Topics in Quantum Electronics*, 23(4):1–7, 2017.

[66] R. Gordon, A. G. Brolo, A. McKinnon, A. Rajora, B. Leathem, and K. L. Kavanagh. Strong polarization in the optical transmission through elliptical nanohole arrays. *Phys. Rev. Lett.*, 92:037401, Jan 2004.

[67] Gediminas Seniutinas, Armandas Balčytis, Yoshiaki Nishijima, Achim Nadzeyka, Sven Bauerdick, and Saulius Juodkazis. Ion beam lithography with gold and silicon ions. *Applied Physics A*, 122(4):383, March 2016.

[68] Martin Wegener. 3d laser nano-printing for bio-scaffolds and metamaterials (conference presentation). In *Laser Applications in Microelectronic and Optoelectronic Manufacturing (LAMOM) XXIII*, volume 10519, page 1051910. International Society for Optics and Photonics, 2018.

[69] Zhaoyang Shen, Helin Yang, Xiaojun Huang, and Zetai Yu. Design of negative refractive index metamaterial with water droplets using 3d-printing. *Journal of Optics*, 19(11):115101, 2017.

[70] Elena Mikheeva, Redha Abdeddaim, Stefan Enoch, Jérôme Wenger, Fabien Lemarchand, Antonin Moreau, Ivan Voznyuk, and Julien Lumeau. Hyperbolic metamaterials based on metal-dielectric thin layers. In *Advances in Optical Thin Films VI*, volume 10691, page 106911T. International Society for Optics and Photonics, 2018.

[71] Huanyang Chen, Che Ting Chan, and Ping Sheng. Transformation optics and metamaterials. *Nature Materials*, 9(5):387, 2010.

[72] Guixin Li, Shuang Zhang, and Thomas Zentgraf. Nonlinear photonic metasurfaces. *Nature Reviews Materials*, 2(5):1–14, 2017. Number: 5 Publisher: Nature Publishing Group.

[73] Sergey Kruk and Yuri Kivshar. Functional meta-optics and nanophotonics governed by mie resonances. *ACS Photonics*, 4(11):2638–2649, 2017. Publisher: American Chemical Society.

[74] Yuri Kivshar. All-dielectric meta-optics and non-linear nanophotonics. *National Science Review*, 5(2):144–158, 2018.

[75] Kirill Koshelev, Andrey Bogdanov, and Yuri Kivshar. Meta-optics and bound states in the continuum. *Science Bulletin*, 64(12):836–842, 2019.

[76] Jeremy Butet, Benjamin Gallinet, Krishnan Thyagarajan, and Olivier JF Marti. Second-harmonic generation from periodic arrays of arbitrary shape plasmonic nanostructures: A surface integral approach. *J. Opt. Soc. Am B*, 30(11):2970–2979, 2013.

[77] Jeremy Butet, Pierre-Francois Brevet, and Olivier J. F. Martin. Optical second harmonic generation in plasmonic nanostructures: From fundamental principles to advanced applications. *ACS Nano*, 9(11):10545–10562, 2015.

[78] J. D. Jackson. *Classical Electrodynamics, 3rd Edition*. Wiley-VCH, 3rd edition edition, 1998.

[79] Bernardo S Mendoza and W Luis Mochán. Exactly solvable model of surface second-harmonic generation. *Physical Review B*, 53(8):4999, 1996.

[80] Jesús A. Maytorena, Bernardo S. Mendoza, and W. Luis Mochán. Theory of surface sum frequency generation spectroscopy. *Phys. Rev. B*, 57:2569–2579, Jan 1998.

[81] P. Guyot-Sionnest and Y.R. Shen. Bulk contribution in surface second-harmonic generation. *Physical Review B*, 38(12):7985–7989, 1988.

[82] Y R Shen. *Principles of nonlinear optics*. Wiley, 1 1984.

[83] Guillermo P. Ortiz, Brenda E. Martínez-Zérega, Bernardo S. Mendoza, and W. Luis Mochán. Effective optical response of metamaterials. *Physical Review B*, 79(24):245132, 2009. Publisher: American Physical Society.

[84] K Glazebrook and F Economou. Pdl: The perl data language. *Dr. Dobb's Journal*, 22(9), 1997.

[85] Stephane Ducasse, Michele Lanza, and Sander Tichelaar. Moose: An extensible language-independent environment for reengineering object-oriented systems. In *Proceedings of the Second International Symposium on Constructing Software Engineering Tools (CoSET 2000)*, volume 4, 2000.

[86] Lucila Juárez-Reyes, Bernardo S. Mendoza, and W. Luis Mochán. Mie scattering in the macroscopic response and the photonic bands of metamaterials. *physica status solidi (b)*, 257(5):1900557, 2020.

[87] SV Popov. *Susceptibility Tensors for Nonlinear Optics*. Routledge, 2017.

[88] Honghua U. Yang, Jeffrey D'Archangel, Michael L. Sundheimer, Eric Tucker, Glenn D. Boreman, and Markus B. Raschke. Optical dielectric function of silver. *Physical Review B*, 91(23), June 2015.

[89] Robert W Boyd. *Nonlinear Optics*. Elsevier, 2003.

[90] Jongwon Lee, Mykhailo Tymchenko, Christos Argyropoulos, Pai-Yen Chen, Feng Lu, Frederic Demmerle, Gerhard Boehm, Markus-Christian Amann, Andrea Alù, and Mikhail A. Belkin. Giant nonlinear response from plasmonic metasurfaces coupled to intersubband transitions. *Nature*, 511(7507):65–69, 2014. Number: 7507 Publisher: Nature Publishing Group.

[91] Yong Zeng, Walter Hoyer, Jinjie Liu, Stephan W. Koch, and Jerome V. Moloney. Classical theory for second-harmonic generation from metallic nanoparticles. *Physical Review B*, 79(23):235109, 2009.

[92] K. Y. Raygoza-Sánchez, I. Rocha-Mendoza, P. Segovia, A. V. Krasavin, G. Marino, T. Cesca, N. Michieli, G. Mattei, A. V. Zayats, and R. Rangel-Rojo. Polarization dependence of second harmonic generation from plasmonic nanoprism arrays. *Scientific Reports*, 9(1):11514, December 2019.

[93] Max Born and Emil Wolf. *Principles of Optics: Electromagnetic Theory of Propagation, Interference and Diffraction of Light*. Cambridge University Press, 7 edition, 1991.

[94] P. B. Johnson and R. W. Christy. Optical constants of the noble metals. *Physical Review B*, 6(12):4370–4379, 1972.

[95] Matthias W. Klein, Martin Wegener, Nils Feth, and Stefan Linden. Experiments on second- and third-harmonic generation from magnetic metamaterials. *Optics Express*, 15(8):5238–5247, 2007. Publisher: Optica Publishing Group.

[96] Cristian Ciracì, Ekaterina Poutrina, Michael Scalora, and David R. Smith. Origin of second-harmonic generation enhancement in optical split-ring resonators. *Physical Review B*, 85(20):201403, 2012.

[97] T. Zentgraf, T. P. Meyrath, A. Seidel, S. Kaiser, H. Giessen, C. Rockstuhl, and F. Lederer. Babinet's principle for optical frequency metamaterials and nanoantennas. *Physical Review B*, 76(3):033407, July 2007.

[98] Tiziana Cesca, Emma Vianey García-Ramírez, Hectór Sánchez-Esquivel, Niccolò Michieli, Boris Kalinic, Juan Manuel Gómez-Cervantes, Raul Rangel-Rojo, Jorge Alejandro Reyes-Esqueda, and Giovanni Mattei. Dichroic nonlinear absorption response of silver nanoprism arrays. *RSC Advances*, 7(29):17741–17747, 2017. Publisher: The Royal Society of Chemistry.

[99] S L Alder. *Physical Review B*, 126:413, 1962.

[100] N Alder. *Phys. Rev.*, 129:62, 1963.

[101] Victor Mizrahi and J. E. Sipe. Phenomenological treatment of surface second-harmonic generation. *Journal of the Optical Society of America B*, 5(3):660, 1988.

[102] J. E. Sipe. New green-function formalism for surface optics. *Journal of the Optical Society of America B*, 4(4):481, 1987.